

Magnetohydrodynamics of Black Holes

Contents

1. Topics	1813
2. Participants	1815
3. Brief description	1817
4. APPENDICES	1819
A. Black hole magnetospheric physics and quasar jets	1821
A.1. Introduction	1821
A.2. Observational Evidence for Black Hole Central Engines	1822
A.2.1. The Kinetic Luminosity of Quasar Jets	1824
A.2.2. Broadband Composite Spectrum: Estimating the Luminosity of the Accretion Flow	1826
A.2.3. The Ultra-Luminous Quasar Sample	1828
A.2.4. Implications for Accretion Flow Driven Jets	1834
A.2.5. The Role of the Black Hole	1835
A.3. Magnetic Flux Configurations Near the Horizon	1837
A.3.1. The ZAMO frames	1838
A.3.2. Poloidal Fields From Current Loops/No Hair Theorem	1839
A.4. Gravito-hydro-magnetics	1843
A.5. 3-D numerical Simulations of Black Hole Magnetospheres . .	1847
A.6. Discussion	1862
Bibliography	1863

1. Topics

- black holes
- galactic gamma ray sources

2. Participants

- B. Punsly (ICRA, ICRANet)

3. Brief description

Most quasars radiate a small fraction of their emission in the radio band (radio quiet), yet about 10% launch powerful radio jets with a kinetic luminosity rivaling or sometimes exceeding the luminosity of the quasar host (radio loud). There is currently no clear theoretical understanding of this bimodality. Empirical reasoning indicates that jets emitted from supermassive black hole magnetospheres are likely required for any theory to be reconciled with the observations. One half of this chapter is dedicated to strengthening the argument that the black hole not the accretion disk is the power source for powerful quasar jets through analysis based on the new large extragalactic databases. The fundamental conclusion is that the jet power is not strongly coupled to the quasar accretion rate. There has been much debate in the literature over the physical mechanism associated with black hole jet creation. The other half of this chapter is devoted to the physics of energy extraction from black hole magnetospheres. There are two theoretical principles, one is gravitohydrodynamics (GHM) which is the theory of how inertial effects of a plasma in the ergosphere can drive a global current system in a jet. The fundamental physics of the ergospheric dynamo is clearly illustrated through snapshots of a numerical simulation. There is a second theoretical mechanism, the Blandford-Znajek mechanism that is purely electrodynamic in nature and is not driven by inertial effects that is only applicable to those magnetic field lines that thread the event horizon and not the equatorial plane of the ergosphere. Recent numerical simulations indicate that an accretion system will evolve to the Blandford-Znajek solution under certain initial conditions. However, the endpoint of these simulations is an electrodynamic jet that is tightly coupled to the accretion state in contradistinction to the observational data presented in the first half of this chapter. The field lines that thread the equatorial plane are governed by GHM. The activation of the GHM ergospheric disk driven jet swamps the electrodynamic jet associated with the event horizon in 3-D numerical simulations as expected on theoretical grounds. It is shown in this chapter that GHM magnetospheres are very successful at explaining the broadband observational data of large samples of quasars, in particular strong jets can be driven by modestly accreting systems.

4. APPENDICES

A. Black hole magnetospheric physics and quasar jets

A.1. Introduction

One of the great mysteries of astrophysics is why a small percentage of quasars radiate bipolar jets that feed huge extended radio lobes on the order of 100 kpc in extent. There is no commonly accepted explanation for the bimodality in quasar intrinsic jet power, but it is believed that either the accretion disk or the black hole is the power source for the jets. What is the mechanism that creates the jets and why does it not occur in most quasars? This chapter is an attempt to shed some light on these issues using the new large quasar and radio source databases combined with some theoretical considerations of black hole magnetospheres.

It is generally believed that the quasars are the luminous manifestations of accretion flows towards supermassive black holes at the heart of an AGN (active galactic nucleus). Local viscous dissipation heats the inflowing gas creating a powerful optical/UV signature that is considered to be well fit by a superposition of thermal spectra that are a consequence of the differential temperature distribution of the gas. It is also commonly believed that much of the accretion energy is reprocessed into emission lines and as IR radiation by the molecular and dusty gas surrounding the central engine. Apparently, there is some physical mechanism that occasionally occurs within this black hole/accretion flow system that can initiate powerful collimated beams of relativistic plasma - the central engine for FRII (Fanaroff-Riley type II) jets.

Section 2 of this chapter examines the important observational evidence that black hole rotation is the most likely power source for the strong FRII jets observed in quasars. The remainder of the chapter is dedicated to reviewing the physical theories of black hole energy extraction by means of large scale magnetic fields. Section 3 describes some possible scenarios and relevant theory involving the distribution of magnetic flux around a black hole, the black hole magnetosphere. The following section reviews the theory of black hole gravitohydrodynamics (GHM) through a new simulation of thin magnetic flux tubes that accrete toward the horizon. This is the inertial process by which large scale magnetic flux through the ergosphere can torque a black hole. These field lines can thread the equatorial plane and therefore not the event horizon. Other more sophisticated 3-D numerical simulations

of strongly accreting systems are also explored. Most of these simulations evolve towards a system in which there is only an electrodynamic horizon jet (i.e., a Blandford-Znajek (B-Z) type solution). However, in certain versions of these 3-D simulations, involving rapidly rotating black holes, a GHM driven jet emerges from the inner part of the accretion flow and the power output of the jet goes up precipitously. In this chapter, we review the nature of these simulations in detail.

A.2. Observational Evidence for Black Hole Central Engines

Simulations and models of jets driven by accretion disks abound in the present day literature. However, there are shortcomings to an accretion disk power source for quasar jets that have led astrophysicists to study black hole driven jets. Firstly, the radio powerful quasars have ultraviolet spectral signatures (spectral index and UV broad line profiles) and luminosity (associated with the local viscous dissipation of the intense gas accretion towards the black hole) that are for the most part indistinguishable from other quasars with feeble radio luminosity. Most of the small intrinsic contrasts in the emission line profiles are well described by differences in a distant intermediate line region that is not directly associated with the accretion flow Corbin and Francis (1994); Brotherton et al (1994). The parsec scale gas of the intermediate line region is likely to be altered significantly by jet propagation Bicknell et al (1998). Intuitively, an accretion disk that describes a quasar like 3C 82 that has over ten times the kinetic luminosity in its jet compared to the broadband (IR to X-ray) luminosity due to viscous dissipation should have a spectrum significantly different than a typical radio quiet quasar (which has about 0.1% of its power in a jet), but its UV spectrum is quite ordinary for a quasar in terms of line widths, spectral index and luminosity Rawlings et al (1989).

This is in stark contrast to the nature of X-ray binaries. These sources have strong correlations between both the spectral index and the luminosity of the thermal X-rays from the accretion disk with radio jet activity Fender (2004). The spectral signature correlation is not a trend that is seen in the quasar population as noted above. Also, for moderate accretion rates, the radio power correlates with accretion luminosity, yet large accretion rates can suppress the jet Fender (2004). Furthermore, there are trends such as spatially resolved jets are triggered by the highest, “super Eddington” accretion episodes Garcia et al (2003). We show in this section that the large jet kinetic luminosity does not require large accretion rates to occur in quasars in contrast to X-ray binaries. In fact we find that there is no switch (such as black hole spin, accretion rate or black hole mass) for the jet associated with the accretion flow in quasars, hence making the case for an accretion disk powered jet seem un-

likely in quasars (in spite of the fact that X-ray binary jets are consistent with being driven by the accretion disk).

Secondly on theoretical grounds, accretion disk models require a significant vertical magnetic flux that gets twisted toroidally in order to launch a powerful, stable, highly collimated jet (for example the quasar 3C 175 has a jet that is collimated to less than 0.7 degrees over 100,000 light years, see Figure 8.1) Wang et al (1990); Benford (1978); Hardee (1996); Meier (1999). One could argue that the magnetic flux that launches the jet is from a different region of the disk than the UV emission, hence avoiding the spectral and luminosity conundrum of accretion disk powered jets noted above. However, this is not viable since most accretion disk models find that the peak of the quasar UV luminosity (1000-2000 Angstroms) is from the inner regions of the accretion disk and this is the only region of the disk that rotates fast enough to drive powerful jets. More fundamentally, since the magnetic flux should flow inwards with the accreting gas, there is really no reason for the accretion disk to attain a large vertical magnetic flux, it is really just a pathway for flux accreting towards the black hole, not a sink for flux. The inference is that the black hole rotational energy, not the accretion flow, is the most likely power source for quasar jets.

The relationship between the central engine of the FR II jets and the black hole/accretion disk system has been a topic of much astrophysical interest for over 20 years Begelman et al (1984). There are three components of the system that have been considered to be related to the launching of powerful radio jets in the past: accretion rate, black hole mass and black hole spin. The results of this section show that even though this three dimensional parameter space can provide some general trending of the radio power within certain quasar sub-populations, it is insufficient for explaining the primary trigger mechanism for FR II jets. A natural choice for a fourth parameter is the accretion of large scale ordered magnetic flux that has been indirectly detected on 100 pc scales in nearby galaxies Jones (2000); Wang et al (1990).

This study considers powerful quasars in order to find clues pertaining to the nature of central engine of strong FR II (Fanaroff-Riley type II) radio sources: is there a switch in the accretion flow that turns on the jet? The strength of a radio source is quantified in this treatment in terms of estimates of kinetic luminosity of the jets that support radio lobe structures as opposed to simply the radio flux density. This is a major improvement over using a flux density at 5 GHz, as is commonly done in the literature for convenience, which can be a very misleading indicator of actual jet power supplied by the central engine. We look at the quasar subset that have the highest known intrinsic thermal optical/UV luminosity. These sources would need extremely large central black holes ($\sim 10^{10} M_{\odot}$) accreting near the Eddington limit in order to support their bolometric thermal luminosity (IR to X-ray, including emission lines). Furthermore, due to the high average accretion rate of this sample, these black holes should have larger spin angular momentum on av-

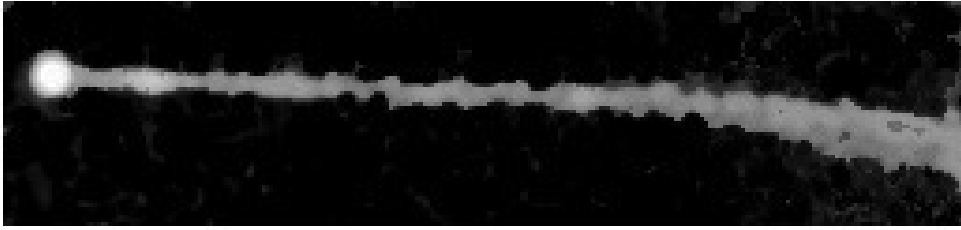


Figure A.1.: The jet from the quasar 3C 175 appears highly collimated in this 5 GHz VLA image provided courtesy of Alan Bridle. The jet terminates in a large lobe of radio emitting plasma that is not shown. The highly collimated region of the jet is over 25 arcsec long which implies a length in excess of 100,000 light years. The jet transports approximately 10^{46} ergs/sec to the radio lobe. The only known collimation mechanism for this narrow beam are large scale toroidal magnetic fields that can be stabilized against pinch instabilities by a large scale axial magnetic field component. The existence of magnetic field is verified by large synchrotron losses from the jet. The original data is from Bridle et al (1994)

erage than the general quasar population. By studying the radio properties of these sources, one can determine if either the central black hole mass, the accretion rate or black hole spin is a trigger for strong radio sources as has been previously conjectured. It is clearly shown that this is not the case. The radio properties of a sample of the most intrinsically luminous quasars (roughly the top 1% in intrinsic optical/UV luminosity in the 10th edition of *Quasars and Active Galactic Nuclei* Veron-Cetty and Veron (2001)) are shown to be remarkably modest at best. This strongly suggests that pure accretion flows in of themselves are not triggers for FR II radio jets, some other physical entity must be present to initiate the jet.

A.2.1. The Kinetic Luminosity of Quasar Jets

The purpose of this section is to discuss various improvements to estimating the power present in the jets compared to the simplistic technique of using flux densities at 5 GHz that is commonly used to assess the radio powers of

quasars within a large sample. A good estimate of the jet power is essential to this study since it can be used to quantify the power emerging from the central engine. In actuality, the radio luminosity is merely an indirect measure of the energy transported through the jets from the central engine that is not directly interpretable. Most of the energy flux is in mechanical form (kinetic luminosity) - the particles and fields necessary to produce the synchrotron luminosity that is detected in the radio lobes. The radiation losses, manifested as radio emission from the jet, are merely the waste energy of this kinematic flow.

Surprisingly, the most difficult methods of estimating jet power rely on observations of the jets themselves. Due to significant Doppler enhancement in relativistic jets, the synchrotron radio emission is a poor indicator of jet intrinsic power. For example, Cygnus A has extremely powerful radio lobes and rather faint radio jets. Most of the energy in the jets is not radiated away, but is transported to the lobes in the classical FR II double lobe morphology. Even the inclusion of observations of high energy emission such as optical or X-ray (inverse Compton) in one's analysis of jet energetics does not tightly constrain the bulk of the jet flow. If the resolution is poor at high frequency (as is often the case) then one can not necessarily associate the plasma emitting the high frequency photons with the radio emitting plasma. If one has high resolution images then the high frequency emission can be detected in enhancement regions or knots in the jets. One can use this information to get an estimate of the plasma conditions within the dissipative knot, but this does not necessarily constrain the plasma state in the bulk of the jet. Furthermore, there are still ambiguities with the Doppler factor that affect the estimates quite dramatically.

The Doppler enhancement of relativistic flows in jets is a crucial parameter since the total luminosity of an unresolved jet scales as the Doppler factor to the fourth power (and to the third power for a resolved cylindrical jet). This is the reason why the implementation of 5 GHz flux densities, as is common in studies of radio loudness of large quasar samples, is a poor indicator of the true intrinsic kinetic luminosity of the jets. More specifically, the majority of core dominated blazar-like quasars have incredibly strong 5 GHz flux densities from emission on the sub-kiloparsec scale, yet they have very weak radio lobe emission. This is interpreted as the jet being necessarily of modest kinetic luminosity (at best) because there is not a large amount of hot plasma and gas that has been transported through the jets to the radio lobes. The 5 GHz flux only represents the dissipation in the jet itself and it has been extremely Doppler boosted. An estimate of kinetic luminosity based on 5 GHz flux density can be off by four or more orders for a core dominated blazar!

A far better way to estimate the kinetic luminosity from a jet is to study the isotropic properties of the material ejected from the ends of the jets in the radio lobes. The radiation from the lobe material is generally considered to be of low enough bulk velocity so that Doppler enhancement is not much

of an issue. The basic idea is that lobe expansion is dictated by the internal dynamics of the lobes and the physical state of the enveloping extragalactic gas. X-ray observations can indicate a bremsstrahlung spectrum of the surrounding gas that can be used to find the pressure of the extragalactic medium. X-rays also provide information on the working surfaces at the end of the lobes, "the hot spots." One can associate the X-ray emission as inverse Compton radiation from the hot spots and the radio luminosity is the synchrotron emission from the hot spots. This constrains the plasma state within the luminous hot spots. However, most of the energy stored in the lobes is in the large diffuse regions of radio emission that constitutes the majority of the large volume of the radio lobes. It is the enormous volume of synchrotron emitting plasma within the lobes ($\sim 10^4 - 10^5 \text{kpc}^3$) that is the most direct indicator that the jets must be supplying huge quantities of hot plasma and magnetic field energy to the lobes.

The most sophisticated calculation of the jet kinetic luminosity requires neither the assumption that the spectral ageing is relevant to the determination of lobe advance speed nor the assumption of minimum energy in the lobes. This method incorporates deviations from the minimum energy estimates in a multiplicative factor f that represents the departure from minimum energy, geometric effects, filling factors, protonic contributions and low frequency cutoff (see Willott et al (1999) for details). The quantity, f is argued to be constrained to be between 1 and 20. In Blundell and Rawlings (2000), it was further determined that f is most likely in the range of 10 to 20. In the following, a standard value of $f = 15$ is chosen for all sources. This allows one to convert 151 MHz flux densities to estimates of kinetic luminosity, Q_{151} , using equation (12) and figure 7 of Willott et al (1999) by means of the following relation:

$$Q_{151} \approx 2 \times 10^{45} \left[\frac{z^2 (1 + \frac{z}{2})^2}{(1+z)^{1-\alpha}} F_{151} \right]^{\frac{6}{7}} \text{ ergs/sec} , \quad (\text{A.2.1})$$

where the flux density at 151 MHz is F_{151} (measured in Janskys), the spectral luminosity is a power law $L_\nu = L_0 \nu^{-\alpha}$ and a cosmological model with $H_0 = 55 \text{ km/sec/Mpc}$ and $q_0 = 0$ is adopted (these parameters are chosen throughout in order to keep contact with the past history of this topic, one is free to change the cosmological model, but it should have minimal consequences to this study).

A.2.2. Broadband Composite Spectrum: Estimating the Luminosity of the Accretion Flow

The most important samples for the composite quasar spectra are the HST observations since these cover the EUV (extreme ultraviolet) region in which

it was once believed that much of the quasar energy was hidden Zheng et al (1997). Figure 1.2 is a composite spectral energy distribution of a radio quiet quasar with $M_V = -25$ (roughly the average value in the Zheng et al (1997) HST sample). This spectrum, in combination with the broad emission lines, represents the “typical” radiative signature of a strong accretion flow onto a black hole in the absence of an FR II jet. This signature is empirical and is independent of all theoretical models of the accretion flow. The broad emission line contribution to the accretion luminosity is difficult to interpret, since it might be strongly affected by the nonaccreting gas dynamics on scales on the order of 0.1 pc from the central black hole and in general any connection to the accretion flow is necessarily indirect.

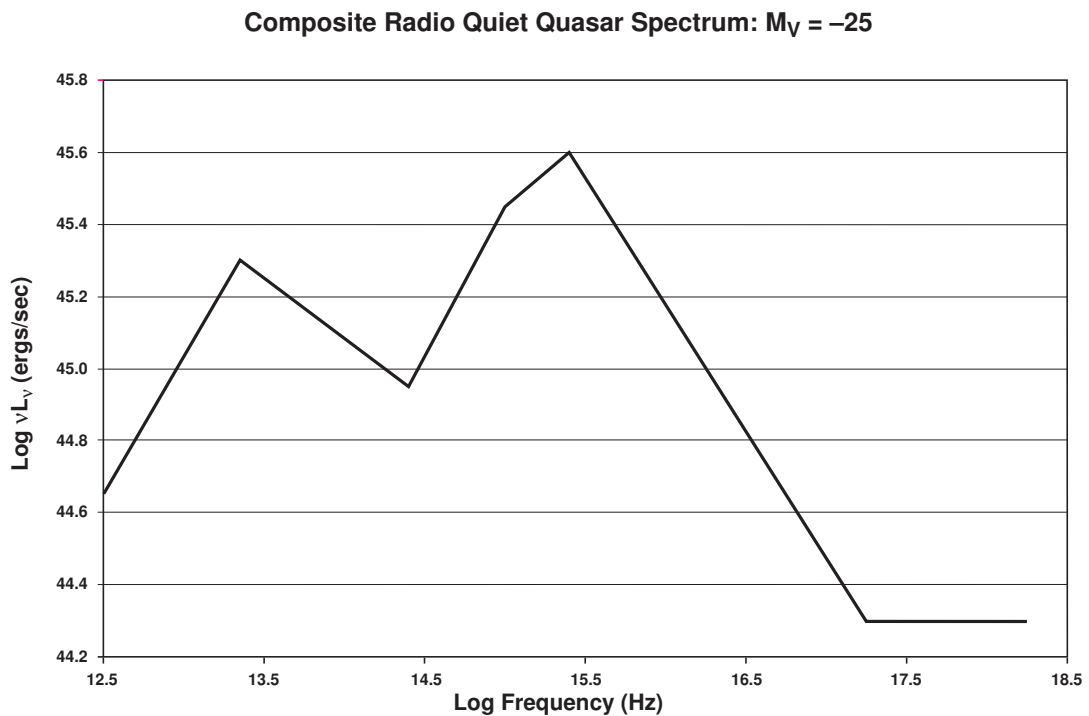


Figure A.2.: The composite spectral energy distribution of a quasar with $M_V = -25$ from the combined data of Elvis et al (1994); Zheng et al (1997); Telfer et al (2002); Laor et al (1997)

Figure 8.2 is a piecewise collection of power laws that approximate the individual bands. The IR and optical data are from the composite spectrum of Elvis et al (1994), the NUV (near ultraviolet) and EUV data are from the HST composites of Zheng et al (1997); Telfer et al (2002) and the X-ray portion of the composite is from Laor et al (1997). One can compute the bolometric luminosity of the accretion flow from the composite spectral energy distribution assuming that 25 percent of the total optical/UV quasar luminosity is reprocessed in the broad line region, $L_{bol} = 1.35 \times 10^{46}$ ergs/sec. If one

also assumes that the shape of the composite spectrum in Figure 8.2 is independent of quasar luminosity, a simple approximate formula is obtained that relates the k-corrected absolute visual magnitude with bolometric luminosity,

$$L_{bol} \approx 10^{\frac{-(25+M_V)}{2.5}} \times 10^{46} \text{ergs/sec} . \quad (\text{A.2.2})$$

This estimator of bolometric luminosity of the accretion flow is a direct measurement of an accretion flow property. Thus, it is superior to using line emission to estimate the accretion flow power which is an indirect estimator. The advantage of using line luminosity is that one can study both FR II radio galaxies (obscured quasars) and quasars in the same sample as in Rawlings and Saunders (1991). However, the down side of using line luminosity is that it is a second order indicator of accretion luminosity. This study is restricted to quasars so it has the advantage that one can use a primary indicator of accretion luminosity such as (8.2).

A.2.3. The Ultra-Luminous Quasar Sample

The sample of quasars chosen is from *A Catalogue of Quasars and Active Nuclei*: 10th edition Veron-Cetty and Veron (2001). This catalogue is suitable for this study because of its large size and the fact that the quasars absolute visual magnitudes have been k-corrected and corrected for line emission that has been redshifted into the observation frequency band. The most optically luminous quasars in the catalogue are of relevance to the discussions of this section. These quasars are the result of the most intense accretion flows onto central black holes. By choosing $M_V < -28.5$, we are left with a large sample of sources quasars that have bolometric luminosity that can be estimated from (8.2), $L_{bol} > 2.5 \times 10^{47} \text{ergs/sec}$. This is above the Eddington luminosity of a $10^9 M_\odot$ black hole. This will be referred to as the ultraluminous quasar sample.

A further restriction on sample selection is also dictated by the desire to get meaningful kinetic luminosity estimates. This study is made practical mainly by the implementation of the very sensitive NVSS survey at 1.4 GHz. The sensitivity is about 2.5 mJy. This survey is restricted to declinations above -40 degrees and therefore, so is our sample. At declinations below this, the PMNJ survey is not sensitive enough to give reasonable upper bounds on the kinetic luminosity for non-detections. In order to get useful upper bounds on the kinetic luminosity of the quasars even with the sensitive NVSS survey, one must bound the maximum redshift as well. For example, assuming a radio spectral index of +1 (corresponding to survey flux sensitivity of 23 mJy when extrapolated to 151 MHz) for a quasar at $z=2$, equation (8.1) implies that an NVSS non-detection would only bound the kinetic luminosity to $Q_{151} < 8.44 \times 10^{44} \text{ergs/sec}$. This bound represents a moderately strong FR II

level kinetic luminosity. Thus, a compromise is made that still allows for a large subsample of bright quasars (123) from Veron-Cetty and Veron (2001) as well as reasonably low bounds on kinetic luminosity: $z < 2$, $\delta > -40$ and $M_V < -28.5$. Thus, most of the black holes in these quasars are super-massive, rapidly spinning with enormous accretion rates. All of the putative switches for radio emission from an accretion disk (mass, accretion rate and black hole spin) should be on for many of the sources!

Radio Properties of the Ultraluminous Quasar Sample

Since limited radio data is available for the sources in the ultraluminous quasar sample, it will be necessary to estimate the jet kinetic luminosity, in general, from a single flux density measurement which is chosen to be the 151 MHz flux used in equation (8.1). The distribution of radio luminosity as a function of k-corrected, visual absolute magnitude is plotted in Figure 8.3. The kinetic luminosity is expressed in units of the kinetic luminosity of Cygnus A that is calculated by the same method.

Note that most points are just upper limits (the arrows). There are three types of upper bounds which are rated from the loosest upper bounds to the tightest upper bounds, below.

1. Some are just nondetections in which the sensitivity of the 151 MHz data is limited by the NVSS or FIRST surveys. There are 81 upper limits of this type in the sample.
2. Many others do not have data at another frequency besides 1.4 GHz, thus one does not know the spectral index. In principle, it is the optically thin contribution to the 151 MHz flux from extended radio emission that is used in the calculation. For core dominated sources, this is difficult to extricate without radio maps at various frequencies. Thus, estimating the 151 MHz optically thin emission from the 1.4 GHz data only yields an upper bound (which could be very close to the actual value if it is a lobe dominated source). There are 13 upper limits of this type in figure 8.3.
3. Many of the stronger sources have photometry at various radio frequencies tabulated in NED. The high frequency data can be used to determine the core spectrum in a two component model of the radio spectrum in which the optically thin extended emission is assumed to have a spectral index of +1. In these instances, a more accurate upper bound can be achieved because the core flux can be subtracted away from the total 151 MHz flux. There are 23 upper limits of this type in the ultraluminous sample.

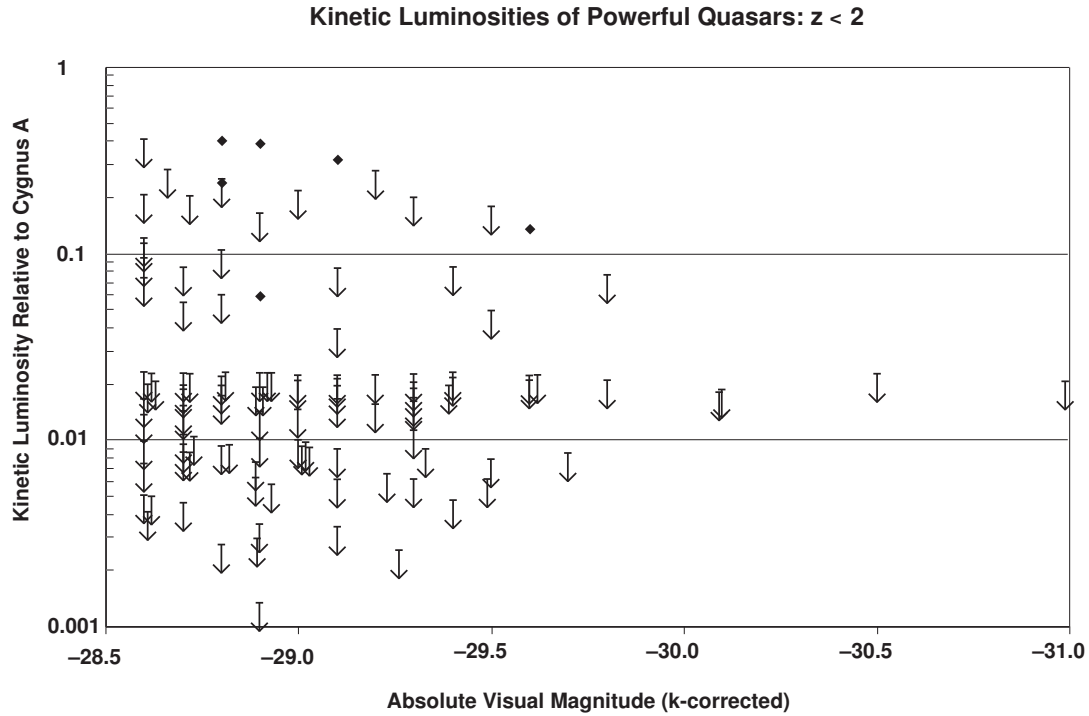


Figure A.3.: The kinetic luminosities of the radio jets of in the sample of ultra-luminous quasars with $z < 2$. The radio data was extracted from the following references available on-line (frequency of measurement in parentheses): NVSS(1.4 GHz), FIRST (1.4 GHz), NASA Extragalactic Database (all frequencies), Kellerman et al (1994) (5GHz), and Veron-Cetty and Veron (2001)(2.7 GHz and 5 GHz). The following catalogs from the NASA Astronomical Data Center were used as well: Texas Survey of Radio Sources (365 MHz), Molonglo Reference Catalogue of Radio Sources (408 MHz), The Fourth Cambridge Survey (4C) (178 MHz), 6C, 7C and 8C Radio Survey (151 MHz), The Parkes-MIT-NRAO (PMN) (4.85 GHz) Survey, The MIT -Green Bank 5 GHz Survey, The Second and Third Bologna Surveys (408 MHz)

For the purpose of this analysis, all three types of upper bounds are treated the same (i.e., the same type of arrow is used because the plot would become too cluttered, otherwise).

The stronger that the radio source is in the sample, the more likely there is a published radio map by selection effects (there are maps for most of the sources with fluxes above 0.5 Jy at 5 GHz and most are core dominated). This is fortunate, because the larger the flux, the larger that the systematic errors can be in the crude estimations discussed above. Also, many of the ultraluminous sources are PG sources and VLA data of these sources were obtained in Kellerman et al (1994). For core dominated blazars in the sample (such as PKS 2134+004, B2 1308+32 and 4C 29.45), the subtraction of the strongly Doppler enhanced emission in the core and in the kpc scale jets requires deep radio images. The procedure for such a subtraction was described in detail for the blazars noted above in Punsly (1995, 1996).

Some of the upper limits in Figure 8.3 are quite large. This occurs either because of a non-detection at high redshift or in sources with powerful radio cores and no radio maps. In the second instance, due to spectral variability of the core it is sometimes difficult to subtract off the core emission properly. In order to remedy this problem somewhat, one can restrict the ultraluminous quasar sample to quasars with a redshift less than 1.5 (see Figure 8.4). This removes most of the high upper limits found in Figure 8.3. Notice that both plots indicate the same message: there are very few sources that are even within an order of magnitude of Cygnus A and there is no evidence of the kinetic luminosity increasing with optical power.

Another useful graphical representation of the data can be found by plotting the ratio of jet kinetic luminosity to the bolometric accretion luminosity, R , versus absolute magnitude. This is done in Figure 8.4 for the $z < 2$ sample and in Figure 8.6 for the $z < 1.5$ sample of ultraluminous quasars. It is very clear that there is no enhancement of the jet with increased accretion power. In fact, it looks as if the quantities are unrelated. Because there are so many upper bound this statement cannot be made with any statistical precision. Certainly there are no Cygnus A type powerhouses that are being triggered by this intense accretion except for 4C 55.27 which is a classical double lobed extended radio source that is 40 % as powerful as Cygnus A Hintzen et al (1983).

Selection Effects Within the Sample

There are certainly selection effects that are present in within the sample of Veron-Cetty and Veron (2001) that could in principle affect the conclusions above. However, as discussed below the strongest selection effects all act to mitigate the strong trends noted above in Figures 8.3-8.6: the conclusions above are actually stronger than indicated by this sample. Firstly, the estimate of the bolometric luminosity in (8.2) from the absolute magnitude does not

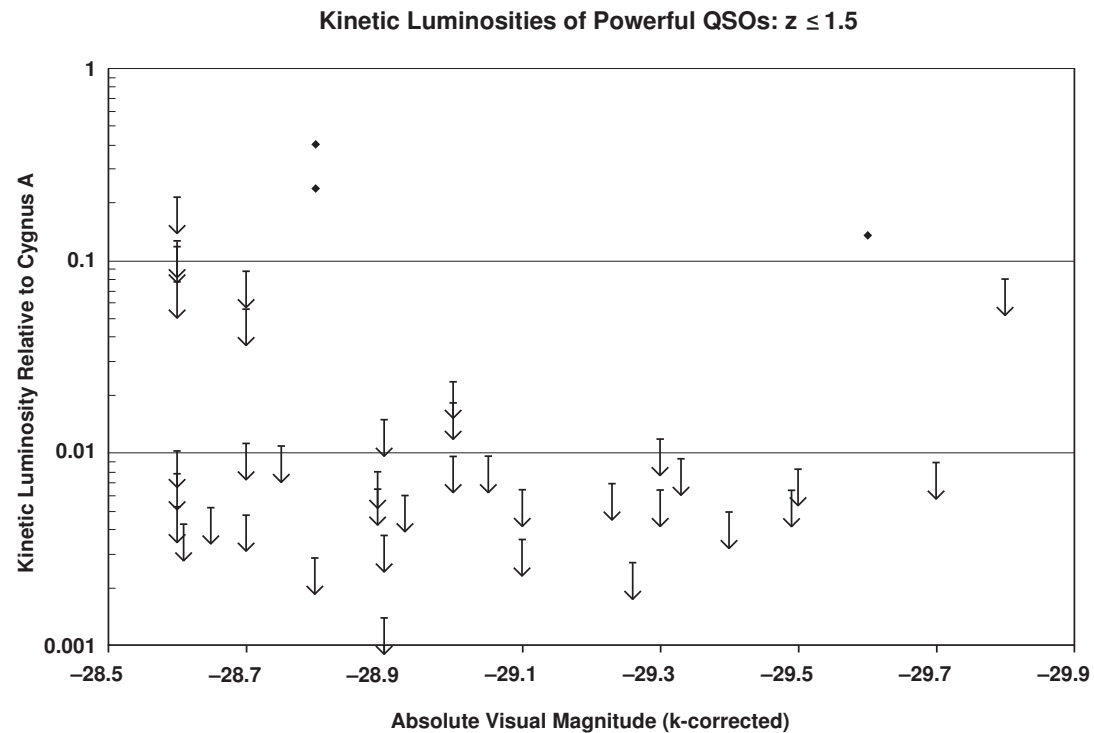


Figure A.4.: The kinetic luminosity of the radio jets of in the sample of ultra-luminous quasars with $z \leq 1.5$

take into account intrinsic reddening in the quasars. Thus, in general L_{bol} is under estimated and the values of R are smaller than those indicated in Figures 8.5 and 8.6.

The stronger radio sources in the sample often have more extensive data available. There is a pronounced tendency for these to be core dominated objects. In blazars, the radio core (which is the unresolved base of the radio jet) has a synchrotron spectrum (that is often self-absorbed at radio frequencies) with a high frequency, steep spectrum tail that can be significant at optical wavelengths. The intrinsic synchrotron emission at optical wavelengths can be enhanced by four orders of magnitude by Doppler enhancement (The apparent flux from an unresolved relativistic plasma will be enhanced relative to the intrinsic value by the Doppler factor raised to the power of $3 + \alpha$. For blazars, Doppler factors of ~ 10 or larger are common). Thus, the absolute magnitude of these sources in the ultraluminous quasar sample can be greatly enhanced over the value that is created by the accretion disk proper Smith et al (1988). The evidence for such an occurrence is high optical polarization or violent optical variability. Many core dominated quasars do not show these effects and the accretion disk is clearly the dominant source of optical emission. It is the other subpopulation of core dominated quasars that can affect the conclusions of this sample. For example, the blazars B2 1308+32

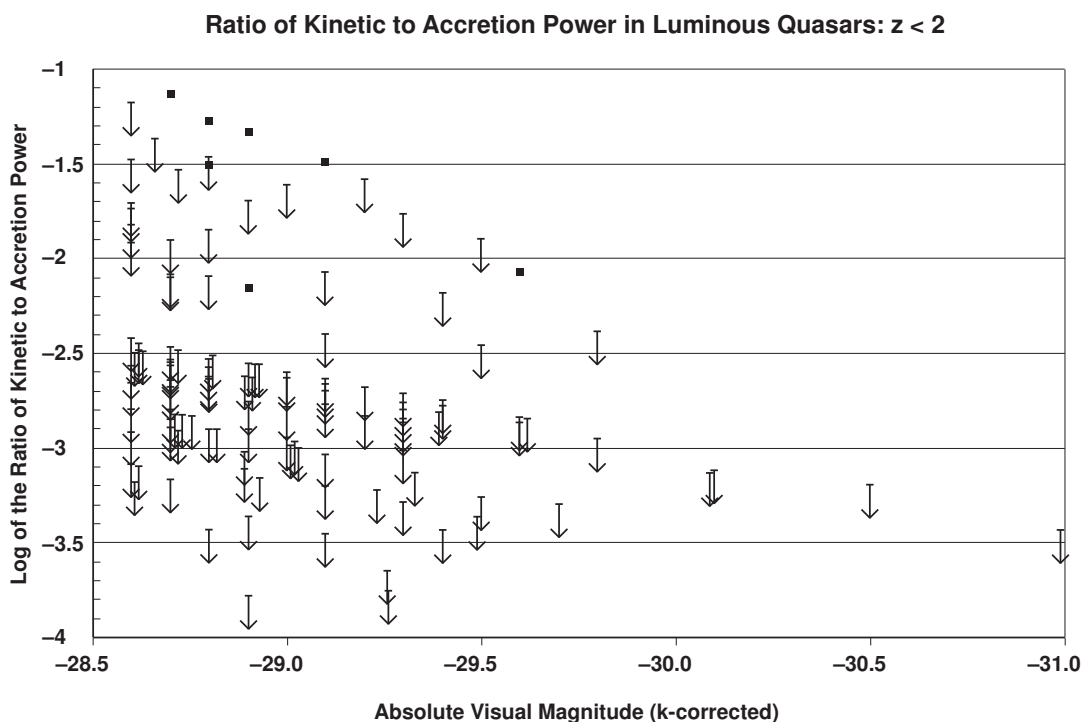


Figure A.5.: The ratio of jet kinetic luminosity to the bolometric luminosity of the quasar accretion flow as a function of absolute magnitude. Note that there is no evidence of a propensity for a quasar to be a strong radio source when the accretion rate becomes large in the $z < 2$ sample of ultraluminous quasars.

and 4C 29.45 have optical polarizations exceeding 10 percent and are highly variable Wills et al (1992). Their absolute magnitudes are -28.6, thus if it weren't for the synchrotron emission from the jets these sources would not make the ultraluminous sample. In particular 4C 29.45 has been analyzed in great detail and the accretion disk contribution to the disk luminosity was found to be less than 3 percent of that which would be predicted from (8.2) and the absolute visual magnitude alone Punsly (1996); Smith et al (1988). The complication is that these are radio sources that should not be in the sample. Furthermore, these two sources would be in the top 5 percent in terms of estimated kinetic luminosities in Figures 8.3 and 8.4. These sources have therefore been removed from the statistical analyses of this sample, so as not to skew the data. Unfortunately there is not enough data on most sources to know the extent of the jet contributions to the optical absolute magnitude, thus there is no systematic way to edit the sample for this type of bias. One can simply note that the kinetic luminosity distribution in the ultraluminous sample is biased to have too many powerful jets due to this selection effect.

Both of the selection effects above indicate that our conclusion based on

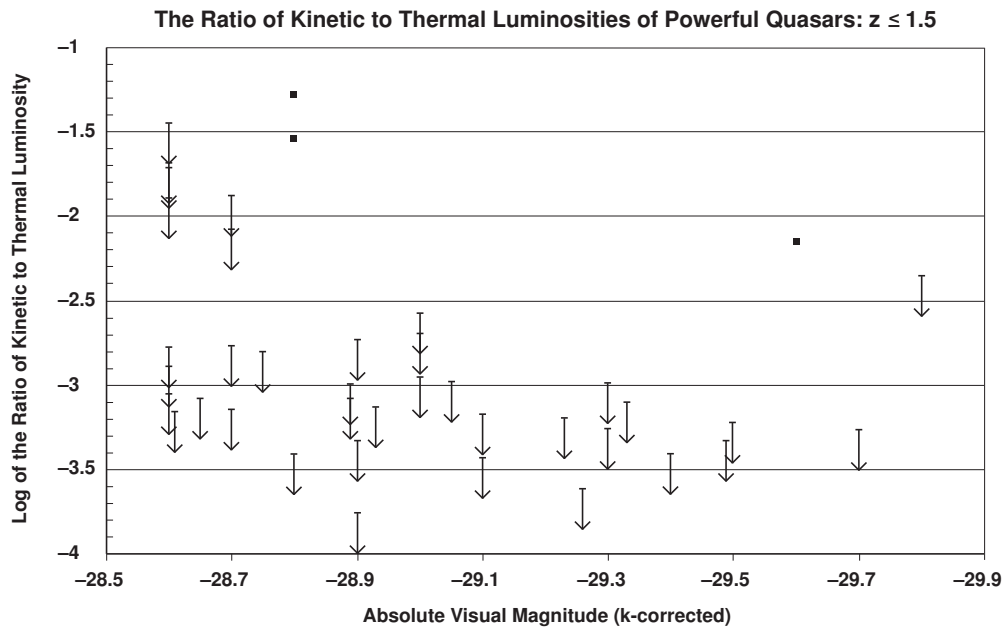


Figure A.6.: The ratio of jet kinetic luminosity to the bolometric luminosity of the quasar accretion flow as a function of absolute magnitude. Note that there is no evidence of a propensity for a quasar to be a strong radio source when the accretion rate becomes large in the $z \leq 1.5$ sample of ultraluminous quasars

Figures 8.3-8.6 that there are very few intrinsically powerful jets amongst the quasars with ultraluminous accretion flows is even stronger in reality than the data reflect.

A.2.4. Implications for Accretion Flow Driven Jets

It is often argued that the accretion flow itself can power FR II jets in quasars. Jets are known to arise from accretion flows in other astrophysical objects such as protostellar disks. However, these jets are quite different from an energetics or a propagation speed standpoint. The basic idea assumes that some combination of properties of the black hole accretion system turns on the quasar jet as it does in the protostellar disk. However, it has been shown previously that there is no property of the spectrum of the UV radiation from the accretion flow of the quasar that correlates with the property of radio loudness. The best example that the jet does not disrupt the accretion flow is the quasar 3C 82 (4C 43.09). At $z=2.87$, it has about 10 times the kinetic luminosity in the jet than the bolometric luminosity of the accretion disk as verified by radio maps, optical spectrum and 200 micron rest frame observations (reprocessed IR). In spite of the kinetic dominance, the spectrum is

totally ordinary for a quasar Rawlings et al (1989). The far UV spectral index = 0.7 which is the average for radio quiet quasars of a similar bolometric luminosity, Telfer et al (2002), and the broad line properties are ordinary as well in the quasar rest frame: CIV FWHM(full width half maximum) = 5,000 km/sec, EW (equivalent width)= 32 Angstroms, Ly α FWHM = 4,500 km/sec, EW = 91 Angstroms (Steve Rawlings private communication based on new higher signal to noise spectrum). This is very difficult for an accretion disk model to explain. The quasar jets such as 3C 82 are in stark contrast to Galactic black hole jets which occur typically when the accretion disk radiation is in what is called a “low-hard” state Fender (2004). Where “hard” refers to the thermal X-ray spectrum emitted from the disk and its corona. The switch-on of the strongest jets is related to the spectral signatures of the accretion flow. For Galactic black holes, the accretion flow is completely disrupted when strong jets are launched Garcia et al (2003); Malzac et al (2004).

Furthermore, it was shown in this section, for the first time, by a statistical analysis of the ultraluminous sample that there is no connection between high quasar bolometric luminosity and radio loudness (in contrast to X-ray binaries). There is also no suppression of radio loudness at high bolometric luminosity (as is the case for many X-ray binaries, Fender (2004)) - figures 8.5 and 8.6 indicate that about 10%-20% of the quasars are radio loud, but only moderate in jet kinetic power. This is perhaps a slight increase in radio power on average than the general quasar population $\sim 10\%$. Furthermore, powerful FR II sources are not excluded by the example of 4C 55.27. A more impressive example is the southern hemisphere source PKS 0743-67 (this source is at too southerly a declination for our sample), with over 10^{47} ergs/sec of both accretion flow bolometric luminosity and jet kinetic luminosity (based on data taken with ATCA in collaboration with Steven Tingay).

In summary, there is no switch (black hole mass, spin or accretion rate) that turns the accretion disk into a jet source. This lack of correlation of jet power with accretion luminosity in quasar is in contrast with X-ray binaries in which strong correlations are found. X-ray binary jets are consistent with the properties of accretion disk driven jets. By contrast, the evidence presented in this Chapter and elsewhere argues strongly against accretion disk powered FR II jets in quasars.

A.2.5. The Role of the Black Hole

One is thus led to the physics of the black hole and the contiguous ergospheric region as a possible way to reconcile the observations and the difficulty of creating a consistent accretion disk central engine. It appears that there must an additional parameter that turns on powerful FR II jets in quasars other than black hole spin, mass or accretion. The most promising additional parameter is a large scale magnetic flux. It has been shown that disk-like

galactic structures can be conducive to the formation of a substantial enhanced vertical magnetic fields. The amplification of the vertical field to mG levels in the region within 150 parsecs from the center of the Galaxy by the physics of the Galactic plane have been discussed in Chandran et al (2000). It has been shown in Jones (2000) that non-spiral galaxies can also have large vertical magnetic fluxes orthogonal to the galactic plane within a few hundred parsecs of the central black hole. In the case of elliptical hosts for powerful radio quasars, it should be noted that the high resolution HST observations of nearby radio loud elliptical galaxies reveal large disk like structures on the order of 100 pc - 1,000 pc (see the pictures of NGC 4261, NGC 7052 and M87 in Punsly (2001)). Thus, one might expect mG vertical magnetic fields within 100 pc of the central black hole in some elliptical galaxies as well. This could be a source of seed flux for a magnetic central engine of the quasar FRII jet.

So far, the black hole has only been discussed in terms of how it effects the efficiency of the accretion flow. A rotating black hole can also, in theory, power the relativistic jets through dynamics in the ergospheric region between the accretion disk and the event horizon. By considering the black hole magnetospheric physics in addition to the accretion flow dynamics in the context of radio loud quasars, one is able to reconcile many of the findings of this chapter.

1. This immediately resolves the conundrum posed by the very "ordinary" quasar spectra generated by the accretion flows in the kinetically dominated quasars. The jet launching region becomes decoupled from the accretion flow, so one does not expect any drastic changes to the signatures of accretion flow in the kinetically dominated quasars in this scenario. The theory of how vertical magnetic flux in the ergosphere can power relativistic jets at the expense of black hole rotational energy is black hole GHM (gravitohydromagnetics), developed in Punsly (2001).
2. In Chapter 10 of Punsly (2001), it is shown that the power in the jet launched by a rapidly rotating black hole by means of black hole GHM interactions is a monotonic increasing function of the magnetic flux through the equatorial plane of the ergosphere inside of the last stable orbit of the accretion disk (see figure 10.13), as well as the spin of the black hole. The surface area of the equatorial plane in the ergosphere is a function of black hole spin, so the magnetic flux through the equatorial plane is not an entirely independent property. Thus, the jet power is largely decoupled from the accretion flow luminosity and black hole mass. The accretion luminosity is only related to the jet power through second order effects that would regulate the spin of the black hole or the magnetic flux transported through the disk to the ergosphere.
3. The maximum achievable jet power from a quasar in black hole GHM

scales linearly with the central black hole mass as can be seen by applying equations (10.10) and (10.12) to the plotted theoretical jet power in Figure 10.13 of Punsly (2001). This is consistent with the observational findings of Dunlop et al (2003) that the maximum jet power scales with black hole mass.

4. The same equations and Figure 10.13 can be used to show that the accretion flow luminosity can be used to derive a linear relation that behaves as an upper bound to the kinetic luminosity in quasars. This is merely a consequence of the fact that the accretion flow ram and radiation pressures regulate the maximum magnetic pressures that are physically allowable in the ergosphere. The maximum jet kinetic luminosity in black hole GHM, Q_{max} , for a given accretion flow luminosity, L_{bol} scales as $Q_{max} \approx 20L_{bol}$ (see equation (10.14) of Punsly (2001)). The linear nature of this upper bound seems to explain the data from the 7C catalogue in Willott et al (1999).

A.3. Magnetic Flux Configurations Near the Horizon

In this section it is demonstrated large scale magnetic flux will not thread the event horizon as charge neutral axisymmetric plasma sources approach the black hole as a consequence of gravitational redshift and the dragging of inertial frames. The metric of the Kerr spacetime (that of a rotating uncharged black hole) in Boyer-Lindquist coordinates, $g_{\mu\nu}$, is given by the line element

$$ds^2 \equiv g_{\mu\nu} dx^\mu dx^\nu = - \left(1 - \frac{2Mr}{\rho^2} \right) dt^2 + \rho^2 d\theta^2 + \left(\frac{\rho^2}{\Delta} \right) dr^2 - \frac{4Mra}{\rho^2} \sin^2 \theta d\phi dt + \left[(r^2 + a^2) + \frac{2Mra^2}{\rho^2} \sin^2 \theta \right] \sin^2 \theta d\phi^2, \quad (\text{A.3.1})$$

$$\rho^2 = r^2 + a^2 \cos^2 \theta, \quad (\text{A.3.2})$$

$$\Delta = r^2 - 2Mr + a^2 \equiv (r - r_+)(r - r_-). \quad (\text{A.3.3})$$

There are two event horizons given by the roots of the equation $\Delta = 0$. The outer horizon at r_+ is of physical interest

$$r_+ = M + \sqrt{M^2 - a^2}. \quad (\text{A.3.4})$$

In Boyer-Lindquist coordinates one can use the four-momentum, P^μ of a particle or plasma to define the mechanical energy, ω , and angular momentum,

m ;

$$\omega = -P \cdot \partial / \partial t , \quad (\text{A.3.5})$$

$$m = P \cdot \partial / \partial \phi . \quad (\text{A.3.6})$$

A.3.1. The ZAMO frames

It is useful to calculate in an orthonormal frame in order to make contact with special relativity. The most useful such frame in the Kerr geometry are the frames of the ZAMOs (zero angular momentum observers), they have zero angular momentum about the symmetry axis of the hole, m . They are the analog of static frames in the Schwarzschild geometry. The zero angular momentum condition requires that they rotate with an angular velocity as viewed from asymptotic infinity, Ω , given by

$$d\phi/dt = \Omega = -g_{\phi t}/g_{\phi\phi} . \quad (\text{A.3.7})$$

The ZAMO basis vectors are determined by the transformation

$$\begin{bmatrix} \hat{e}_0 \\ \hat{e}_\phi \end{bmatrix} = \begin{bmatrix} |g_{tt} - \Omega^2 g_{\phi\phi}|^{-1/2} & \Omega |g_{tt} - \Omega^2 g_{\phi\phi}|^{-1/2} \\ 0 & 1/\sqrt{g_{\phi\phi}} \end{bmatrix} \begin{bmatrix} \tilde{e}_t \\ \tilde{e}_\phi \end{bmatrix} , \quad (\text{A.3.8})$$

$$\hat{e}_r = \left(\frac{\Delta}{\rho^2}\right)^{1/2} \tilde{e}_r = \left(\frac{\Delta^{1/2}}{\rho^2}\right) \frac{\partial}{\partial r} , \quad (\text{A.3.9})$$

$$\hat{e}_\theta = \left(\frac{1}{\rho}\right) \tilde{e}_\theta = \left(\frac{1}{\rho}\right) \frac{\partial}{\partial \theta} , \quad (\text{A.3.10})$$

where we will designate Boyer-Lindquist evaluated quantities by tildes throughout the remainder of the text. The basis covectors are

$$\begin{bmatrix} \omega^0 \\ \omega^\phi \end{bmatrix} = \begin{bmatrix} |g_{tt} - \Omega^2 g_{\phi\phi}|^{1/2} & 0 \\ -\Omega\sqrt{g_{\phi\phi}} & \sqrt{g_{\phi\phi}} \end{bmatrix} \begin{bmatrix} dt \\ d\phi \end{bmatrix} , \quad (\text{A.3.11})$$

$$\omega^r = \left(\frac{\rho^2}{\Delta}\right)^{1/2} dr , \quad (\text{A.3.12})$$

$$\omega^\theta = \rho d\theta . \quad (\text{A.3.13})$$

The gravitational redshift of the ZAMO frames as viewed from asymptotic infinity is a very useful quantity, α , called the lapse function:

$$\alpha = \left| g_{tt} - \Omega^2 g_{\phi\phi} \right|^{1/2} = \frac{\Delta^{1/2} \sin \theta}{\sqrt{g_{\phi\phi}}} . \quad (\text{A.3.14})$$

$$(\text{A.3.15})$$

Note that

$$\lim_{r \rightarrow \infty} \alpha = +1 , \quad (\text{A.3.16})$$

$$\lim_{r \rightarrow r_+} \alpha = 0 . \quad (\text{A.3.17})$$

Thus, α is a valuable dimensionless parameter for expanding quantities in the vicinity of the event horizon, $\alpha \gtrsim 0$.

One of the computational advantages of the ZAMO orthonormal frame is that it is defined only up to a rotation in the (r, θ) plane. In the study of magnetized plasmas it is useful to define a rotated ZAMO basis in which the unit vector \hat{e}_1 is parallel to the poloidal component of the magnetic field, B^P . In terms of the Maxwell tensor in the ZAMO frames,

$$B^1 \equiv B^P = F^{2\phi} , \quad \text{and} \quad B^2 = F^{\phi 1} = 0 . \quad (\text{A.3.18})$$

The basis vectors in the (r, θ) plane become

$$\begin{bmatrix} \hat{e}_1 \\ \hat{e}_2 \end{bmatrix} = \frac{1}{|B^P|} \begin{bmatrix} F^{\theta\phi} & F^{\phi r} \\ -F^{\phi r} & F^{\theta\phi} \end{bmatrix} \begin{bmatrix} \hat{e}_r \\ \hat{e}_\theta \end{bmatrix} . \quad (\text{A.3.19})$$

Using $B^r = F^{\theta\phi}$, and $B^\theta = F^{\phi r}$ the basis covectors in the rotated ZAMO frame are (note: $B^P = \sqrt{(B^\theta)^2 + (B^r)^2}$)

$$\begin{bmatrix} \omega^1 \\ \omega^2 \end{bmatrix} = \frac{1}{|B^P|} \begin{bmatrix} B^r & B^\theta \\ -B^\theta & B^r \end{bmatrix} \begin{bmatrix} \omega^r \\ \omega^\theta \end{bmatrix} . \quad (\text{A.3.20})$$

This basis essentially reduces the dimensionality by one in many calculations.

A.3.2. Poloidal Fields From Current Loops/No Hair Theorem

A common electromagnetic source expected to occur in magnetospheres are loops of azimuthal current. A method for calculating the vacuum fields of electromagnetic sources is given in Punsly (2001) Chapter 4. Consider an identical pair of azimuthal current loops that are accreting towards the black hole as depicted in figures 8.7-8.9. A pair of loops was chosen to represent

an extended source of azimuthal current. The field at the horizon is dominated by the $l = 1, m = 0$ moment of the electromagnetic field on the Kerr background for all axisymmetric sources. The loops are released from rest at $r = 1.4r_+$ in figure 8.7. At a later time, the current loop has approached even closer to the event horizon and the field is depicted in figure 1.8. Notice that the poloidal magnetic field is being redshifted away. The large scale magnetic flux is almost completely gone by figure 8.9. This is the essence of a no hair theorem that all large scale fields from charge neutral electromagnetic sources are redshifted away as they approach the horizon. The pure charge component of a general accreting source contributes only the $l = 0, m = 0$ component of the electromagnetic field (the Kerr-Newman electromagnetic field) as the horizon is approached. It is debatable whether the pure charge component is significant in quasars in which electric fields can be quenched by the plentiful plasma.

There is a second physical mechanism that also switches off the poloidal magnetic field of accreting charge neutral sources that arises from the dragging of inertial frames. This can be shown by looking at the equations of motion of the electromagnetic sources. Asymptotically, one can write out the momentum equation in the ZAMO frame and it is dominated by the gravitational connection, regardless of the initial velocity that is assumed to exist near the event horizon. Asymptotically, the ZAMO connection is

$$\begin{aligned} \Gamma^r_{00} &\sim \alpha^{-1}, & \Gamma^\theta_{00} &\sim \alpha^0, & \Gamma^r_{\phi 0} = \Gamma^r_{0\phi} &\sim \alpha^0, \\ \Gamma^r_{\theta\theta} &\sim \alpha^1, & \Gamma^r_{\phi\phi} &\sim \alpha^1, & \Gamma^\theta_{\phi 0} = \Gamma^\theta_{0\phi} &\sim \alpha^1, \\ \Gamma^\theta_{\phi\phi} &\sim \alpha^0, & \Gamma^\theta_{rr} &\sim \alpha^0, \end{aligned} \tag{A.3.21}$$

and $\Gamma^r_{00} \sim \alpha^{-1}$ when $a = M$ except in the equatorial plane, where $\Gamma^r_{00} \sim \alpha^0$.

Consequently, as $\alpha \rightarrow 0$, the radial gravity dominates in the effective ZAMO gravity, g :

$$g \approx (u^0)^2 \Gamma^r_{00}, \quad \alpha \rightarrow 0. \tag{A.3.22}$$

It is straightforward to show that g always dominates over other forces near the event horizon if one considers the equations of motion of the individual species of charge (the sources for Maxwell's equations) simultaneously with the single fluid equations (see details in chapter 3 of Punsly (2001)). Hence the plasma effectively has infinite inertia in a global sense as seen by frames that are not in free fall at the horizon, i.e., astrophysical observers. The equations of motion can be written in terms of proper time, τ near the horizon

as

$$\frac{du^r}{d\tau} + \Gamma^r_{00} (u^0)^2 \approx 0, \quad (\text{A.3.23})$$

$$\frac{du^0}{d\tau} - \Gamma^r_{00} u^0 u^r \approx 0. \quad (\text{A.3.24})$$

These equations integrate in the ZAMO frames to give the following components of the four-velocity, u^μ and three-velocity \mathbf{v} ,

$$u^0 \sim \alpha^{-1}, \quad (\text{A.3.25})$$

$$v^r = \frac{u^r}{u^0} \sim -1 + \mathcal{O}(\alpha^2), \quad (\text{A.3.26})$$

$$v^\phi = \frac{u^\phi}{u^0} \sim \alpha, \quad (\text{A.3.27})$$

$$v^\theta = \frac{u^\theta}{u^0} \sim \alpha. \quad (\text{A.3.28})$$

By inverting (8.10)-(8.15), one finds that (8.27)-(8.30) imply, in the stationary frames at asymptotic infinity (Boyer-Lindquist coordinates),

$$\tilde{u}^t \sim \alpha^{-2}, \quad (\text{A.3.29})$$

$$\frac{d\phi}{dt} = \Omega_H [1 + \mathcal{O}(\alpha^2)], \quad \Omega_H = \frac{a}{2Mr_+} \quad (\text{A.3.30})$$

$$\frac{dr}{dt} = -\frac{\Delta}{r_+^2 + a^2} [1 + \mathcal{O}(\alpha^2)], \quad (\text{A.3.31})$$

$$\lim_{t \rightarrow \infty} (r - r_+) = \text{constant} \times e^{-2\kappa t}, \quad \kappa = \frac{\sqrt{M^2 - a^2}}{r_+^2 + a^2}, \quad (\text{A.3.32})$$

where Ω_H is the angular velocity of the horizon as viewed in the stationary frames at asymptotic infinity and κ is the surface gravity at the horizon.

The additional physics due to frame dragging of the sources in the red-shifted current rings in figure 8.9 can be understood in terms of the horizon boundary condition above. The azimuthal current in the ZAMO frame is obtained by subtracting the momentum equation of the negative charges from that of the positive charges and multiplying by the charge of a positron. It was assumed in computing figures 8.7-8.9 that the total ZAMO evaluated current was a constant. However, in the inner ergosphere there is an asymptotic scaling with lapse function as a consequence of (8.29),

$$I_\phi \underset{\alpha \rightarrow 0}{\sim} \alpha. \quad (\text{A.3.33})$$

Similarly, in the stationary frames both species of charge must corotate with the horizon, thus there are vanishing azimuthal particle drifts. Thus, globally

the current appears to be turning off as $\alpha \rightarrow 0$,

$$\tilde{I}_\phi \underset{\alpha \rightarrow 0}{\sim} \alpha^2. \quad (\text{A.3.34})$$

Note that the time dilation seen in the ZAMO frame implies that I_ϕ is approximately constant near the horizon in the proper frame of the in-falling ring as expected.

In summary, the black hole wants the plasma, but doesn't want the vertical magnetic flux. Thus, a very likely magnetospheric configuration is one in which the mG vertical flux accretes from 100pc scales towards the hole. Only a very small fraction reaches the ergosphere. The flux tubes accrete close to the horizon where the field reconnects allowing plasma to fall into the hole, leaving vertical flux in the ergosphere (see chapter 8 of Punsly (2001) for details. If one part in 10^{-6} of the vertical flux survives the trip down to the stationary limit, one would expect a vertical magnetic field strength of about 10 G at the stationary limit. Consider a maximally rotating ($a = M$), supermassive black hole, $M = 10^9 M_\odot$. If the average lifetime of an ergospheric flux tube is about 1000 M (the time for a flux tube to accrete to the reconnection zone near the horizon and either resistively diffuse out of the ergosphere or reconnect with an oppositely directed magnetic flux tube), we would expect a field strength of over 10^3 Gauss to accumulate near the event horizon, even if the flux is not trapped inside the ergosphere for long periods of time. However, flux can be pinned close to the horizon by GHM forces of the pressures of the accreting gas leading to even stronger magnetic field strengths in the ergosphere (see Narayan et al (2003)).

It is important to introduce the concept of the field line rotation rate for the study of frozen-in (perfect MHD plasmas). By the frozen-in condition and the definition of the rotated ZAMO basis, there is flow only along the magnetic field lines,

$$u^P = u^1, \quad u^2 = 0, \quad F^{\mu\nu} u_\nu = \forall \mu. \quad (\text{A.3.35})$$

It is instructive to define a frame that corotates with the magnetic field at a fixed radial coordinate "r". The "corotating frame" has a four velocity \bar{u}_μ . The frozen-in condition in this frame becomes

$$F^{20} \bar{u}_0 + F^{2\phi} \bar{u}_\phi = 0. \quad (\text{A.3.36})$$

$$(\text{A.3.37})$$

The azimuthal velocity of the field as viewed by a ZAMO is

$$\beta_F^\phi = \frac{\bar{u}_\phi}{\bar{u}^0}, \quad (\text{A.3.38})$$

$$F^{20} = \beta_F^\phi B^P. \quad (\text{A.3.39})$$

One can define a field line angular velocity, Ω_F , as viewed from asymptotic infinity by a simple basis transformation

$$\beta_F^\phi = \left(\frac{\Omega_F - \Omega}{c\alpha} \right) \sqrt{g_{\phi\phi}}. \quad (\text{A.3.40})$$

Since $\Omega \rightarrow 0$ as $r \rightarrow \infty$ and $\Omega \rightarrow \Omega_H$ as $r \rightarrow r_+$ in a flux tube, $\beta_F^\phi \rightarrow +\infty$ as $r \rightarrow \infty$ and $\beta_F^\phi \rightarrow -\infty$ as $r \rightarrow r_+$, if $0 < \Omega_F < \Omega_H$.

A.4. Gravitohydromagnetics

The GHM interaction is one in which significant inertia is required in order for accreting plasma to conform with the horizon boundary condition, (8.32): all plasma corotates with the horizon as it approaches the black hole. This is actually a gradual condition that occurs because of the dragging of inertial frames throughout the ergosphere. In particular the plasma angular velocity, $d\phi/dt$, is bounded by

$$\Omega_{\min} \leq \Omega_p \leq \Omega_{\max}, \quad (\text{A.4.1})$$

$$\Omega_{\min} = \Omega - c\alpha/\sqrt{g_{\phi\phi}}, \quad (\text{A.4.2})$$

$$\Omega_{\max} = \Omega + c\alpha/\sqrt{g_{\phi\phi}}, \quad (\text{A.4.3})$$

$$\lim_{r \rightarrow r_+} \Omega_{\min} = \Omega_H, \quad \lim_{r \rightarrow r_+} \Omega_{\max} = \Omega_H, \quad (\text{A.4.4})$$

$$\Omega_{\min} > 0 \quad \Rightarrow \quad g_{tt} > 0. \quad (\text{A.4.5})$$

The Penrose process of energy extraction from a black hole operates by sending $\omega < 0$ particles or plasma into the black hole Penrose (1969). This process is fundamental to the physics of GHM. The preparation of plasma with a Boyer-Lindquist energy $\omega < 0$ must occur within the ergosphere. This is related to the fact that the outer boundary of the ergosphere, the stationary limit at $r = r_s$ occurs when $\partial/\partial t$ changes from a timelike vector field to a spacelike vector field. This change happens when g_{tt} switches sign. The outer boundary of the ergosphere is the stationary limit,

$$r_s = M + \sqrt{M^2 - a^2 \cos^2 \theta}. \quad (\text{A.4.6})$$

The physics of relevance to black hole energy extraction occurs within the ergosphere. This is clearly shown by the following calculation. The transformations (8.10) and (8.13) yields an expression for ω , the redshifted energy as

viewed from asymptotic infinity:

$$\omega = \mu u^0 \left[\frac{\Omega_{\min}}{c} \sqrt{g_{\phi\phi}} - (1 + \beta^\phi) \frac{\Omega}{c} \sqrt{g_{\phi\phi}} \right], \quad (\text{A.4.7})$$

$$\beta^\phi = \frac{u^\phi}{u^0} = \frac{(\Omega_p - \Omega) \sqrt{g_{\phi\phi}}}{\alpha c}, \quad (\text{A.4.8})$$

where, Ω_p is the angular velocity of the plasma. The derivation above shows the connection between local counter-rotation, $m < 0$, $\beta^\phi \approx -1$, and the negative energy states, $\omega < 0$. Anticipating the significance of these relativistic counter rotating states,

$$\lim_{\beta^\phi \rightarrow -1} \omega = -\mu u^0 \frac{\Omega_{\min}}{c} \sqrt{g_{\phi\phi}}. \quad (\text{A.4.9})$$

Note that by (8.47), $\Omega_{\min} > 0$ in the ergosphere. Thus, by (8.51), if the plasma has $\beta^\phi \approx -1$ then it will have a negative global energy, $\omega < 0$, and the negative energy states only exist in the ergosphere. Furthermore, the condition on the three-velocity in (8.51) implies a large Lorentz factor and therefore a large inertia has been imparted to the plasma by the relativistic effects of frame dragging.

The GHM interaction will be studied in terms of a numerical simulation of the accretion of a magnetic flux tube that was performed by Vladimir Semenov and Sergey Dyadechkin from the Institute of Physics at the State University of St. Petersburg. They use a method based on the nonlinear string approximation to the perfect MHD magnetic flux tube (see Semenov et al (2002) for details). Consider a vertical flux tube in which the initial velocity of the plasma is that of the local ZAMO observer. The flux tube will begin to accrete toward the black hole. The simulation occurs about a rapidly spinning black hole with $a/M = 0.995$. The equation of state is chosen as $P \sim \rho^2$ and $P \sim (r - r_+)^{-2}$, where P is the total pressure, gas and magnetic. This parametric dependence was chosen for simplicity. The fundamental physics of energy extraction and jet production is quite independent of the pressure function and the initial conditions. When it first penetrates the ergosphere it appears twisted as in Figure 8.10.

Initially, $d\phi/dt = \Omega_0 \equiv \Omega \ll \Omega_H$, since the flux tube is far from the event horizon. The flux tube accretes towards the black hole under the influence of the gravitational force. The “natural state” of plasma motion (geodesic motion) induced by frame dragging is to spiral inwards faster and faster as the plasma approaches corotation with the event horizon (frame dragging). By contrast, the “natural state” of plasma motion in a magnetic field is a helical Larmor orbit that is threaded onto the field lines. In general, these two “natural states” of motion are in conflict near a black hole. The torsional struggle between these two strong forces is the dynamical effect that drives

the simulation depicted in Figures 8.10-8.13. The plasma far from the hole is still rotating slowly near $d\phi/dt \approx \Omega_0$ in Figure 8.10. However, inside the ergosphere, Ω_{min} is necessarily a significant fraction of Ω_H , by (8.44) and Ω_p must exceed Ω_0 in short order. Thus, the ergospheric plasma gets dragged forward, azimuthally, relative to the distance portions of the flux tube, by the gravitational field. The back reaction of the field is an attempt to keep the plasma threaded on the field lines (Larmor helices) by torquing the plasma back onto the field lines with $\mathbf{J} \times \mathbf{B}$ forces (the cross-field current density, \mathbf{J} , driven by this torsional struggle is sunk within the enveloping magnetosphere). By Amperes law, the current driven by the global torsional struggle also makes a negative azimuthal magnetic field, B^ϕ , upstream of the current flow.

The $\mathbf{J} \times \mathbf{B}$ back reaction forces driven by the global torsional struggle simultaneously torque the plasma in the flux tube in the ergosphere. Figures 8.11 and 8.12 show that the B^ϕ created in the ergosphere propagates upstream in the form of an MHD plasma wave at later times, as more and more negative energy is created in the ergospheric region of the flux tube. The negative energy (indicated by the red portion of the magnetic flux tube) is the total plasma energy including both the electromagnetic and the mechanical components of the plasma. In Figures 8.11-8.13, a jet emerges from the ergosphere. The magnetic tower created by B^ϕ in combination with the poloidal field component, B^P , naturally provides stable hoop stresses that are the only known collimation mechanism for the jet morphology of quasars (Hardee 1996; Benford 1978)

The dynamo region for B^ϕ in the ergosphere is expanded in the bottom frame of figure 8.11. Since $B^\phi < 0$ upstream of the dynamo, from the frozen-in condition expressed in (8.41) and the transformation (8.42), there is an electromagnetic energy flux ($\sim -\Omega_r B^\phi B^P$) and an electromagnetic angular momentum flux ($\sim -B^\phi B^P$) along B^P , away from the hole in the jet. The red portion of the field line indicates the total plasma energy per particle, $E < 0$,

$$E = \omega + S/k, \tag{A.4.10}$$

downstream of the dynamo, where S is the Poynting flux, k is the particle flux downstream of the dynamo and the mechanical energy, ω , was defined in (8.7). Since $B^\phi > 0$ downstream of the dynamo in figure 8.11, the field transports energy and angular momentum towards the hole with the inflowing plasma. Thus, $S/k > 0$ in the downstream state. Consequently, $\omega \ll 0$ in order for $E < 0$, downstream. The $\mathbf{J} \times \mathbf{B}$ back reaction forces in the torsional battle torque the plasma onto trajectories with $\Omega_p \approx \Omega_{min}$. The ingoing $\omega \ll 0$ plasma extracts the rotational energy of the hole since $\beta^\phi \approx -1$ as noted in (8.51) and global angular momentum of the plasma defined in (8.8)

is simply expressed in the ZAMO frames as

$$m = u^0 \beta^\phi \sqrt{g_{\phi\phi}}, \quad (\text{A.4.11})$$

which implies that $m \ll 0$ when $\beta^\phi \approx -1$. Thus, black hole rotational inertia is powering the jet in the simulation.

This is precisely the physics of the Penrose process Penrose (1969). Penrose envisioned that a particle could be split into two pieces in the ergosphere. A negative energy ingoing particle extracts the rotational energy of the hole and an outgoing particle goes off to infinity. Thus, energy is extracted from the black hole. In the GHM process the negative energy particles is the torqued plasma in the global torsional struggle. The outgoing particle is a nonlinear MHD wave that can be almost pure Poynting flux.

The physics that was found is related to the fact that the spacetime around a black hole is essentially rotating and so are the particles. This frame dragging force is actually very strong, to overcome it one must overwhelm the rotational inertia of the black hole $\sim 0.1Mc^2$. Thus, the black hole can impart a huge relativistic inertia to any plasma in order to enforce the constraints of frame dragging, the field is overwhelmed regardless of its strength and is twisted and spun-up as necessary generating the Poynting flux that powers the jet.

It is expected that a typical black hole magnetosphere would drive a jet with the same GHM physics. The dynamics of the simulations are not a consequence of any the simplifying assumptions used in the string formalism. The main effect of the enveloping magnetosphere would be to compress or rarify the flux tubes and change their inclination. We have a library of simulations indicating that the same basic physics of jet production exists independent of flux tube inclination, the external pressure function and the value of the pure Alfven speed, $U_A = B^P / \sqrt{4\pi n\mu}$ (in the simulation of Figures 8.10-8.13, the Poynting flux emerges from a region which is magnetically dominated with $U_A = 12 - 13$). Thus, the entire magnetosphere that is found by solving the transverse force equations should be many thin flux tubes that are pieced together at various inclination angles and with various Alfven speeds and pressures. Therefore, it is not surprising that qualitatively similar results are obtained in MHD simulations of an entire black hole magnetosphere in Camenzind and Khanna (2000); Koide et al (2002); Koide (2003).

We expect that most of the vertical flux gets temporarily anchored in the inner ergosphere Igumenshchev et al (2003); Narayan et al (2003). Eventually, the plasma reconnects the field and falls into the horizon as argued in the last section. The amount of flux through the horizon should be negligible (but, see the discussion of the next section). Let us return to the flux estimate that we might expect from the scenario of the accretion of mG large scale flux from 100 pc scales that was discussed at the end of the last section. The flux, Φ , through the equatorial plane of the ergosphere of a rapidly rotating su-

permissive black hole, $M = 10^9 M_\odot$, should be about 10^{33} - 10^{34} G-cm² if the accretion efficiency allows only one part in 100,000 of the field to make it to the ergosphere. The poloidally directed Poynting flux, S^P from in a bipolar pair of jets launched by the ergospheric dynamo should be (assuming relativistic outflow)

$$S^P \approx \frac{(\Omega_F \Phi)^2}{2\pi^2 c} . \quad (\text{A.4.12})$$

The field line angular velocity varies from 0 at r_s to $\Omega_H = 10^{-4} \text{sec}^{-1}$ at r_\pm in the ergosphere. Thus, the GHM mechanism would produce $\sim 10^{45} - 10^{47}$ ergs/sec of Poynting flux from the ergosphere of a supermassive black hole if the vertical flux was accreted from 100 pc scales with an efficiency of 0.00001. This is equivalent to the kinetic luminosity in powerful FR II quasars. Detailed GHM models in Punsly (2001) and references therein yield similar results.

A.5. 3-D numerical Simulations of Black Hole Magnetospheres

There are new impressive simulations of Hirose et al (2004); De Villiers et al (2005a); Krolik et al (2005); Hawley and Krolik (2006) that assume no black hole magnetosphere in the initial state, just an unstable toroid of plasma threaded by concentric loops of weak magnetic flux. There is a fixed amount of plasma in the problem and no additional plasma accretes from large distances in the simulation. As these loops accrete they get twisted in the equatorial plane and stretched by a strong pressure gradient outside the disk, so that the field lines are almost radial as they approach the horizon. The key point is that the outward forces in the disk atmosphere essentially evacuates the flux tube of plasma as it stretches it out. The field lines are deposited near the horizon with very low plasma density. These three-dimensional simulations in De Villiers et al (2003); Hirose et al (2004); De Villiers et al (2005a,b); Krolik et al (2005); Hawley and Krolik (2006) show Poynting flux emanating from magnetically dominated funnels inside of the vortices of thick accretion flows. The simulations are long term ending at $t = 8080M - 10,000M$.

Figure 8.14 is a plot of the time averaged and azimuthally averaged Poynting flux in one of these simulations known as KDE that is distinguished by a near maximal black hole spin, $a/M = 0.998$. This false color contour map indicates a region of strong outgoing Poynting flux in the evacuated funnel at latitudes $30^\circ < \theta < 55^\circ$ near the horizon. It was shown in Punsly (2006a) that most of the the radial Poynting flux, S^r , is created within a layer close to the horizon at $r \approx 1.3M - 1.5M$. Inspection of the contour map indicates that over 70% of the Poynting flux is created within a thin layer near $r \approx 1.4M$. Because of the saturation of the dark red color in the plotting routine, the

Poynting flux is likely to be much larger above the switch-off layer than indicated in the contour map. Thus, we only have a conservative lower bound on the strength of the Poynting flux above the switch-off layer and it is likely that more than 90% of the energy flux is created within this thin layer. There is apparently a small electrodynamic residual source that one could associate with the Blandford-Znajek mechanism.

This phenomenon was explored further in Punsly (2007a). The source of most of the Poynting flux was clearly shown to be outside the event horizon in KDE Punsly (2006a). However, without access to the original data, the details of the physical mechanism could not be ascertained. A second generation of 3-D simulations were developed in Hawley and Krolik (2006), the highest spin case was KDJ, $a/M = 0.99$, with by far the most powerful Poynting jet within the new family of simulations; three times the Poynting flux (in units of the accretion rate of mass energy) of the next closest simulation KDH, $a/M = 0.95$. The last three data dumps, at simulation times, $t = 9840 M$, $t = 9920 M$ and $t = 10000 M$, were generously made available to this author. The late time behavior of the simulations is established after $t = 2000 M$ (when the large transients due to the funnel formation have died off) making these data dumps of particular interest for studying the Poynting jet Hawley and Krolik (2006). The origin of the Poynting jet at these late times was studied in Punsly (2007a) and continues to be studied in collaboration with Shigenobu Hirose and Igor Igumenshchev (as we will discuss below).

The analysis of the data from the KDJ simulation clearly indicates that the Poynting flux in the outgoing jet is dominated by large flares. Typically, one expects the turbulence in the field variables to mask the dynamics of Poynting flux creation in an individual time slice of one of the 3-D simulations Punsly (2006a). Surprisingly, the flares are of such a large magnitude that they clearly stand out above the background field fluctuations as evidenced by Figure 8.15. The flares are created in the equatorial accretion flow deep in the ergosphere between the inner calculational boundary at $r=1.203 M$ and $r= 1.6 M$ (the event horizon is at $r= 1.141 M$). Powerful beams of Poynting flux emerge perpendicular to the equatorial plane in the ergospheric flares and much of the energy flux is diverted outward along approximately radial trajectories that are closely aligned with the poloidal magnetic field direction in the jet (see Figure 8.15). The situation is unsteady, whenever some vertical magnetic flux is captured in the accretion flow it tends to be asymmetrically distributed and concentrated in either the northern or southern hemisphere. This hemisphere then receives a huge injection of electromagnetic energy on time scales $\sim 60M$.

The source of Poynting flux in KDJ resembles a nonstationary version of the ergospheric disk (see Punsly and Coroniti (1990) and chapter 8 of Punsly (2001) for a review). The ergospheric disk is modeled in the limit of negligible accretion and it is the most direct manifestation of gravitohydrodynamics (GHM) Punsly (2001). A GHM dynamo arises when the magnetic field im-

pedes the inflow of gas in the ergosphere, i.e., vertical flux in an equatorial accretion flow. The strong gravitational force will impart stress to the magnetic field in an effort to move the plasma through the obstructing flux. In particular, the metric induced frame dragging force will twist up the field azimuthally. These stresses are coupled into the accretion vortex around a black hole by large scale magnetic flux, and propagate outward as a relativistic Poynting jet. The more obstinate the obstruction, the more powerful the jet. There are two defining characteristics that distinguish the GHM dynamo from a Blandford-Znajek (B-Z) process, Blandford and Znajek (1977), on field lines that thread the ergosphere:

1. The B-Z process is electrodynamic so there is no source within the ergosphere, it appears as if the energy flux is emerging from the horizon. In the GHM mechanism, the source of Poynting flux is in the ergospheric equatorial accretion flow.
2. In a B-Z process in a magnetosphere shaped by the accretion vortex, the field line angular velocity is, $\Omega_F \approx \Omega_H/2$ (where Ω_H is the angular velocity of the horizon) near the pole and decreases with latitude to $\approx \Omega_H/5$ near the equatorial plane of the inner ergosphere Phinney (1983). In GHM, since the magnetic flux is anchored by the inertia of the accretion flow in the inner ergosphere, frame dragging enforces $d\phi/dt \approx \Omega_H$. One therefore has the condition, $\Omega_F \approx \Omega_H$.

In Figure 8.15 we show a false color plot of the radial Poynting flux, S^r , in KDJ in Boyer-Lindquist coordinates (same as Figure 8.14 for KDE). The data is averaged over azimuth at $t=10,000 M$. Overlaid are arrows that indicate the direction (not magnitude) of the azimuthally averaged poloidal Poynting vector. Notice that the strong band of S^r in red originates near the equatorial dense plasma, where the GHM effects power the Poynting flux beam. The Poynting flux creation in this simulation is discussed in depth in Punsly (2008) that is due out in September 2008. As these powerful GHM driven energy beams propagate outward, the energy flux diffuses towards the pole filling the entire jet. Furthermore, it was shown in Punsly (2007a) that $\Omega_F \approx \Omega_H$ in the jets that emerge from the equatorial plane which is characteristic of GHM as noted above.

A secondary aspect of this strong GHM driven jet is that it swamps any Blandford - Znajek process as shown in Punsly (2007b). These simulations have led us to a new realization, the boundaries of the EHM (The event horizon magnetosphere, EHM, is comprised of poloidal flux that threads the event horizon) should be dynamic and are not likely to be passive boundary surfaces for the magnetic field. It was shown that electrodynamic energy flux can arise in the EHM as a result of sources radiating energy from the lateral boundaries. Even if the EHM can be construed as "force-free," the dynamics of the lateral boundaries are determined by strong inertial forces that

should make them strong MHD pistons. This circumstance was not anticipated in theoretical treatments of electrodynamic jets in the EHM Blandford and Znajek (1977); Phinney (1983). The fact that electromagnetic energy can come into the EHM from the side goes right to the heart of the assumptions in the B-Z solution. The B-Z solution is the perfect MHD solution in which energy conservation reduces to Poynting flux conservation from the horizon to a relativistic wind at asymptotic infinity Phinney (1983). From this condition, the parameters of the field are uniquely determined for a given poloidal field distribution, in particular the field line angular velocity, Ω_F , and the total electromagnetic energy output from the black hole, $\int S^r d\theta d\phi$. However these 3-D simulations demonstrate that if there are strong sources of Poynting flux along the lateral walls of the EHM, the spacetime near the event horizon can not adjust the system to enforce the B-Z field parameters within the EHM. This is a direct consequence of the fact that the plasma near the event horizon in the EHM can not effectively react back on the outgoing wind or jet and modify its electromagnetic properties because of the gravitational redshifting of the MHD characteristics Punsly (2001); Punsly and Bini (2004). The plasma near the horizon in the EHM will passively accept any field parameters imposed by the EDJ and the accretion disk corona Punsly (2001). As such, in a general astrophysical context, the basic parameters such as Ω_F and $\int S^r d\theta d\phi$ are indeterminate.

It has become apparent that these 3-D simulations can have complex magnetic field geometries and figures like Figure 8.15 are insufficient. Thus, a collaboration with Shigenobu Hirose and Igor Igumenshchev was begun that uses a 3-D visualizer, Paraview 3.0. Figure 8.16 is a time slice of KDJ at $t=9920$ M in an isometric view (30 degrees south of the equator). The azimuthally twisted field lines magnetic field lines carry Poynting flux from the accreting gas to form a jet. Notice that they originate in the false color density contours outside of the event horizon. This is the effective ergospheric disk in this high accretion rate simulation. The field lines are color coded. The blue lines originate near the equator or above the equator of the event horizon and pass through the gas. As they pass through the accreting gas they form low density magnetic islands and extract energy from the accreting gas. The low density regions can achieve negative specific energy and extract black hole energy as it accretes. This reproduces the Penrose process of GHM even in this high accretion rate environment (see Punsly (2008) for details). The red and green lines are characterized by a toroidal magnetic field that switches direction near the equatorial plane. The northern half (above the point at which $B^T = 0$) of red lines spiral within the accreting gas and never escape, the southern half connect to the large scale southern jet. The green lines connect to both the northern and southern hemisphere jets. This type of diverse inhomogeneous structure is masked in 2-D azimuthal averages as in Figure 8.15.

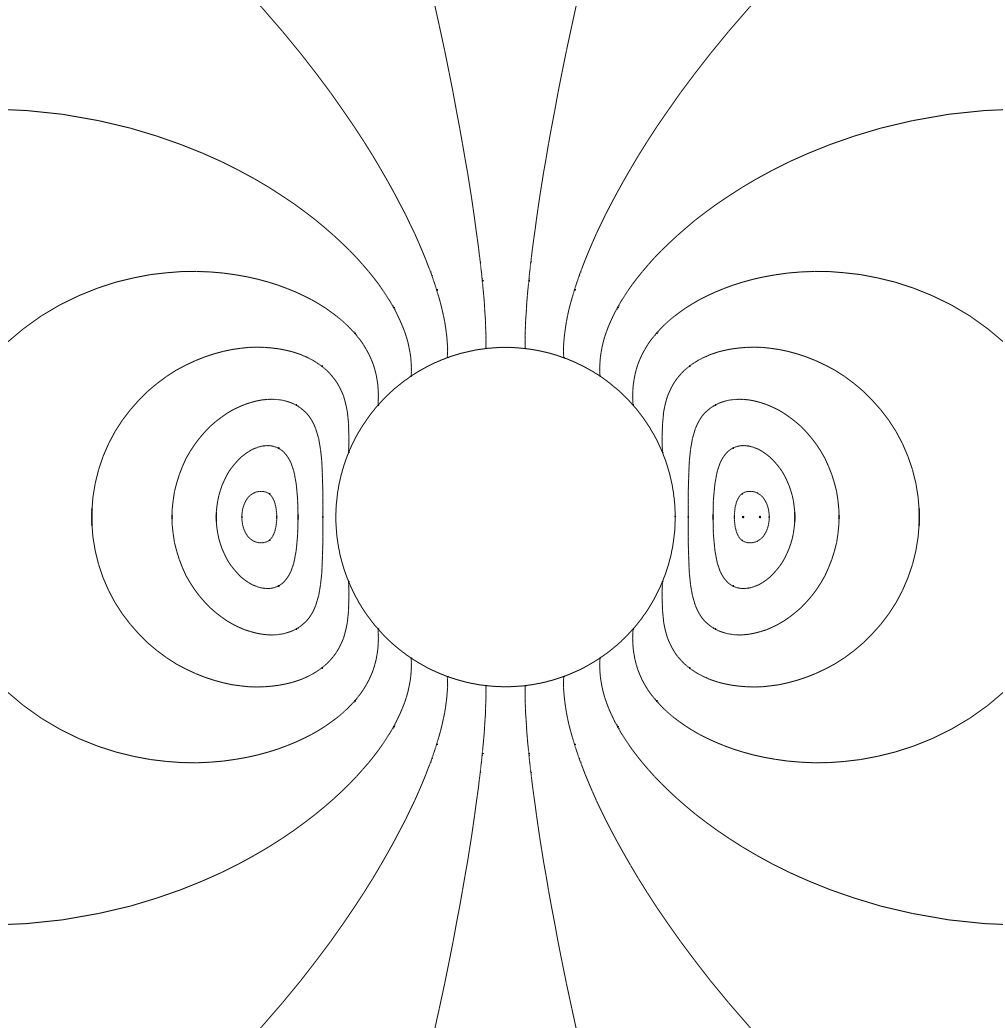


Figure A.7.: The magnetic field of an identical pair of azimuthal current rings near a black hole rotating with $a/M=0.90$. The current rings are initially centered about $r = 1.4r_+$, where they released from rest. The two dots on the right side of the figure represent cross-sections of the azimuthal current loops. The figure was provided courtesy of Tomas Ledvinka

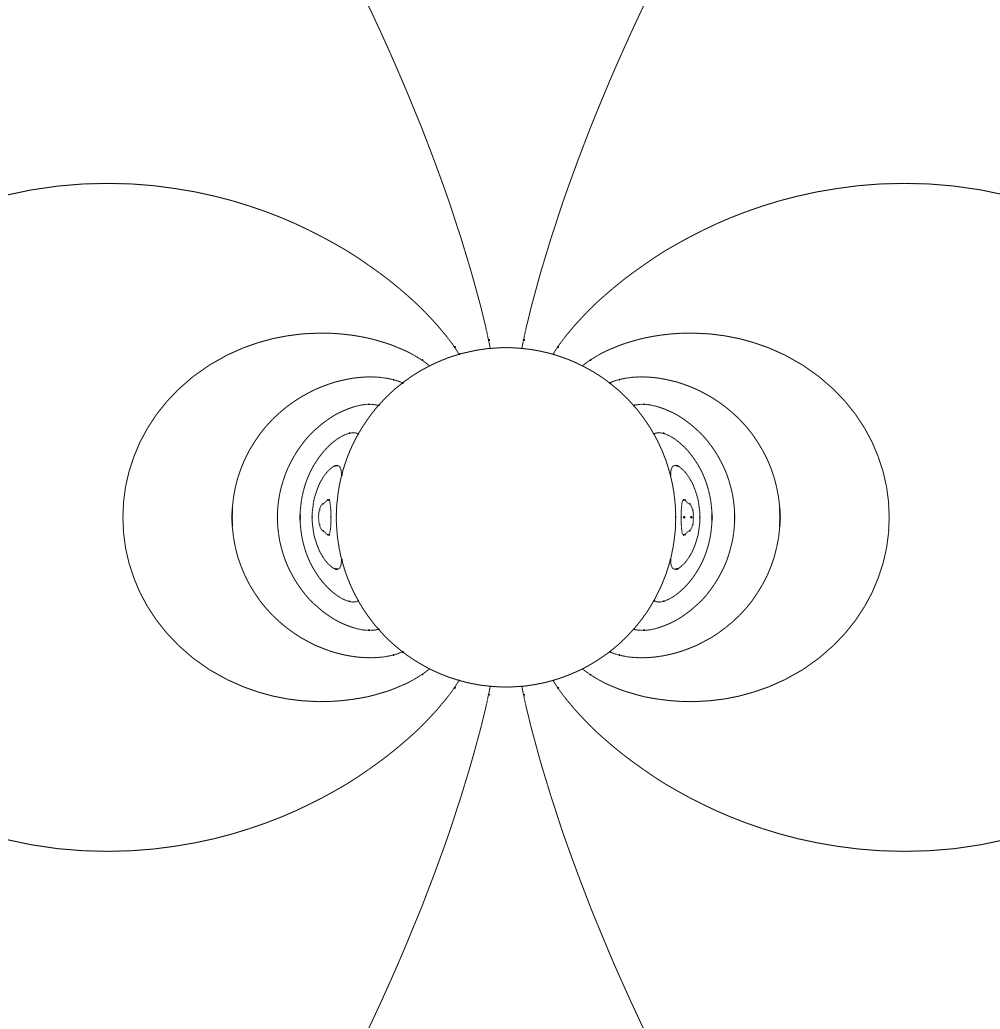


Figure A.8.: The magnetic field of the azimuthal current rings after they have accreted deep into the ergosphere. The inner ring is located at $r = 1.05r_+$. Notice how much weaker the large scale flux is than it was in figure 8.7. The figure was provided courtesy of Tomas Ledvinka

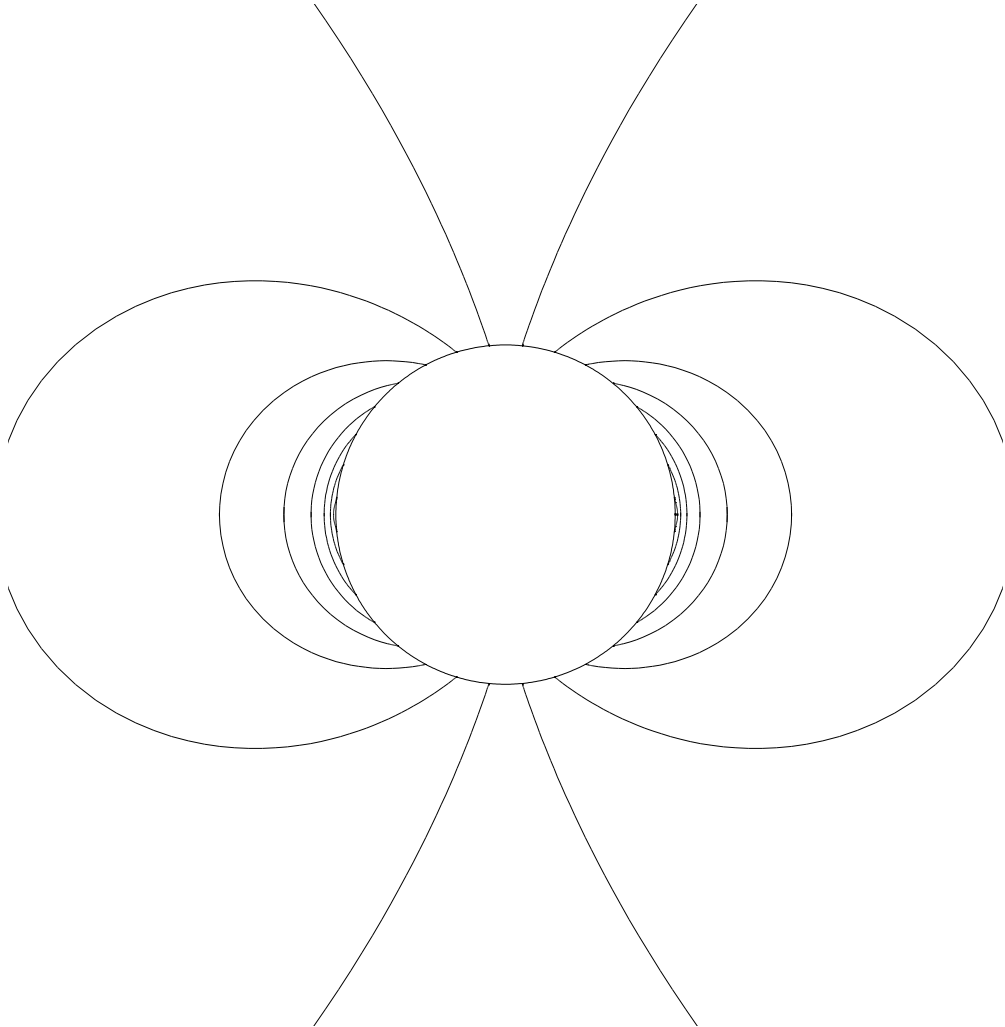


Figure A.9.: The magnetic field from the pair of azimuthal currents when the inner ring has reached $r = 1.001r_+$. The large scale magnetic flux is virtually gone. The figure was provided courtesy of Tomas Ledvinka

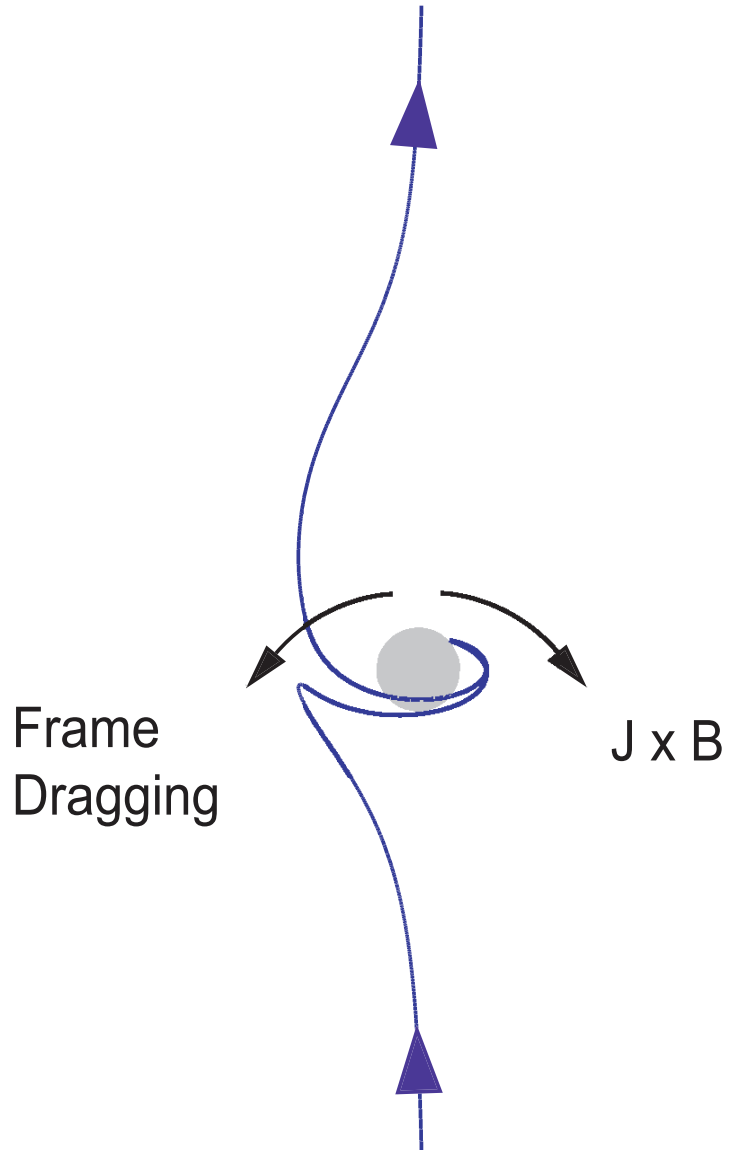


Figure A.10.: The magnetic flux tube experiences a torsional struggle between inertial forces and electromagnetic forces as it enters the ergosphere

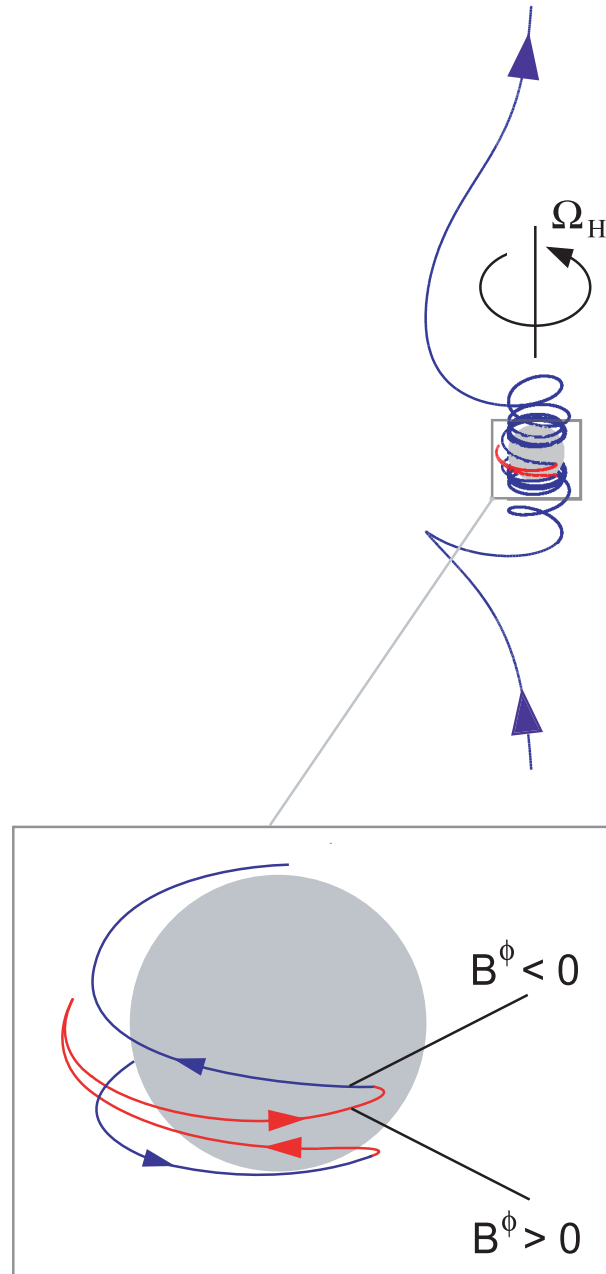


Figure A.11.: The red portions of the field line indicate plasma with negative energy, as viewed globally. The back reaction of the field in the torsional battle torques plasma onto negative energy trajectories while simultaneously creating an outgoing Poynting flux in the jet. The details are described in the text. The time lapse between frames, as measured by a distant stationary observer from figure 8.10 to figure 8.11 is $t = 85.7GM/c^3$. Note that The flux tube rotates in the same sense as the black hole. The bottom frame is a close-up of the dynamo region for the toroidal flux in the jet.

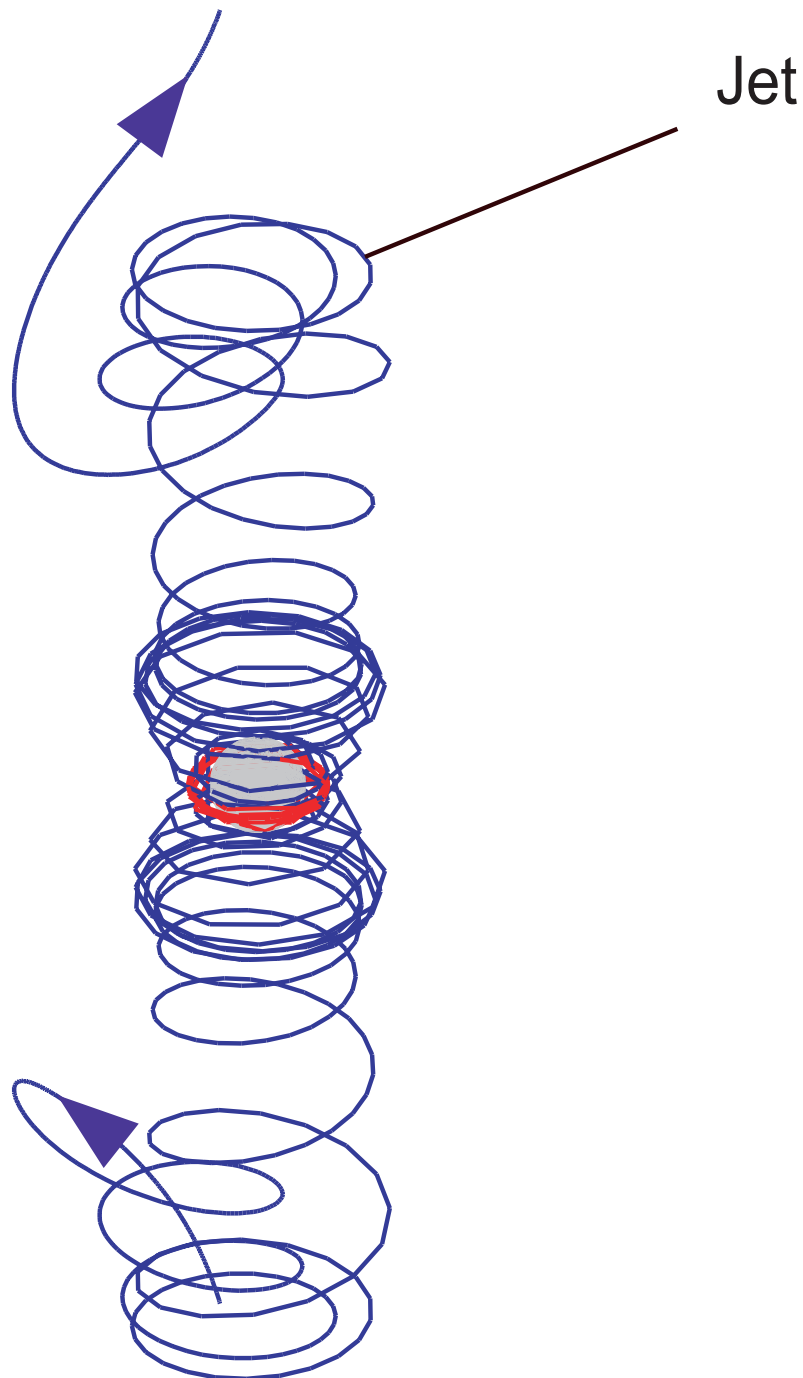


Figure A.12.: A jet is produced on the magnetic flux tubes that experience the ergospheric torsional struggle between frame dragging forces and $\mathbf{J} \times \mathbf{B}$ forces. The Boyer-Lindquist time lapse from figure 8.10 to figure 8.12 is $t = 133.2GM/c^3$.



Figure A.13.: A well-formed jet emerges from the horizon at late times. The Boyer-Lindquist time lapse from figure 8.10 to figure 8.13 is $t = 265GM/c^3$ with a pair of jets with lengths of over $60GM/c^2$. The plasma has attained an outflow Lorentz factor of a little less than 2 in the late stages

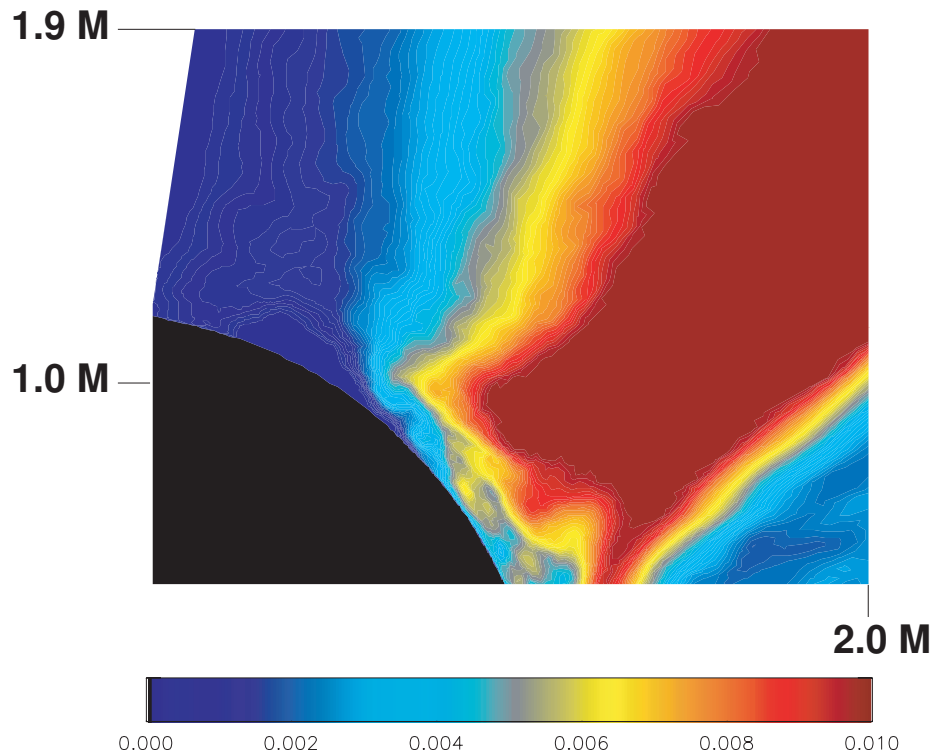


Figure A.14.: The azimuthally averaged and time averaged (over 75% of the simulation that ends at $t = 8080M$) Poynting flux from the model KDE ($a/M = 0.998$) of Krolik et al (2005). The figure is from Punsly (2006a) and is a magnification of the inner region of figure 10 of Krolik et al (2005). It is an excision of a region a little larger than the ergospheric portion of the magnetically dominated funnel that occupies latitudes $0^\circ < \theta < 55^\circ$ near the horizon and the plot spans $0^\circ < \theta < 65^\circ$ near the horizon. The majority of the Poynting flux is created in a layer of cross-field current driven by GHM processes near $r = 1.3M - r = 1.5M$ (see Krolik et al (2005) for a description of the units on the color bar). This region is a source for the majority of the outgoing Poynting flux emerging from the funnel. The grid size is adequate for resolving the Poynting flux source in the switch-off layer, ranging from a mesh size of $\approx 0.001M$ at the inner boundary, $r = 1.175M$, to $\approx 0.01M$ at $r = 1.5M$ according to a cosh function dependence. The plot is provided courtesy of John Hawley

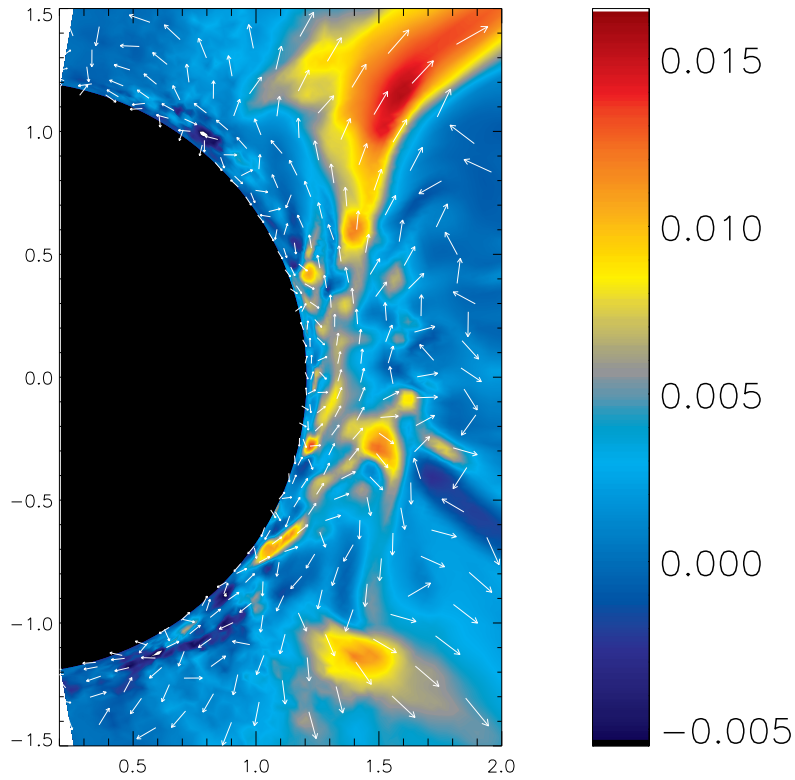


Figure A.15.: The source of Poynting flux, A plot of S^r in KDJ, averaged over azimuth, at $t= 10000 M$. The relative units (based on code variables) are in a color bar to right. The inside of the inner calculational boundary ($r=1.203 M$) is black. The calculational boundary near the poles is at 8.1° and 171.9° . Notice that any contribution from an electrodynamic effect associated with the horizon appears minimal. The arrows indicate the direction of the poloidal Poynting vector

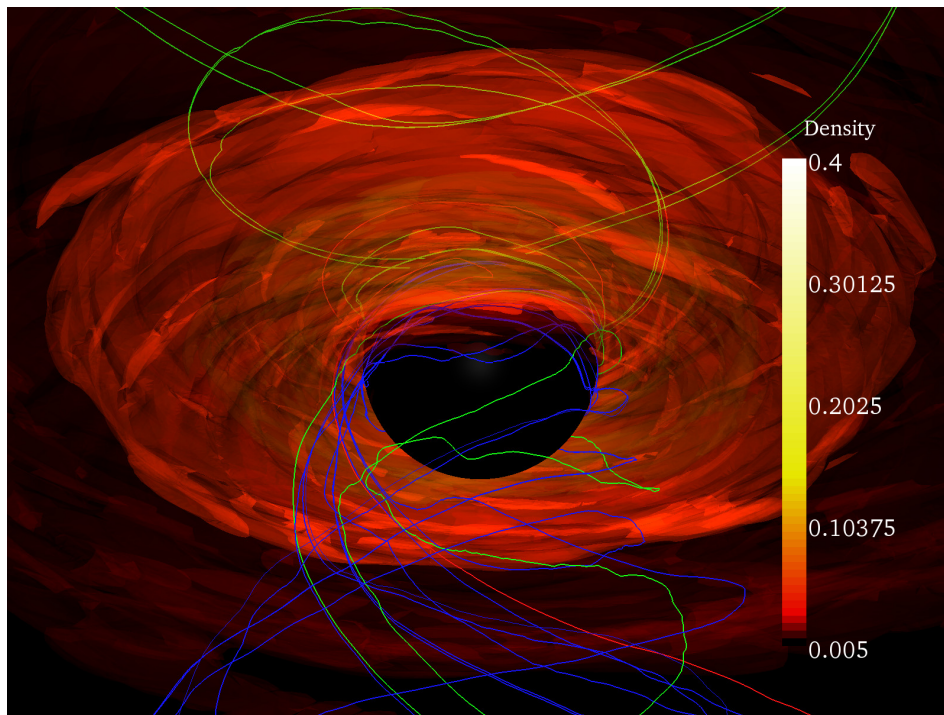


Figure A.16.: Magnetic field lines are superimposed on the false color density contours in this time slice of KDJ, $t = 9920 M$

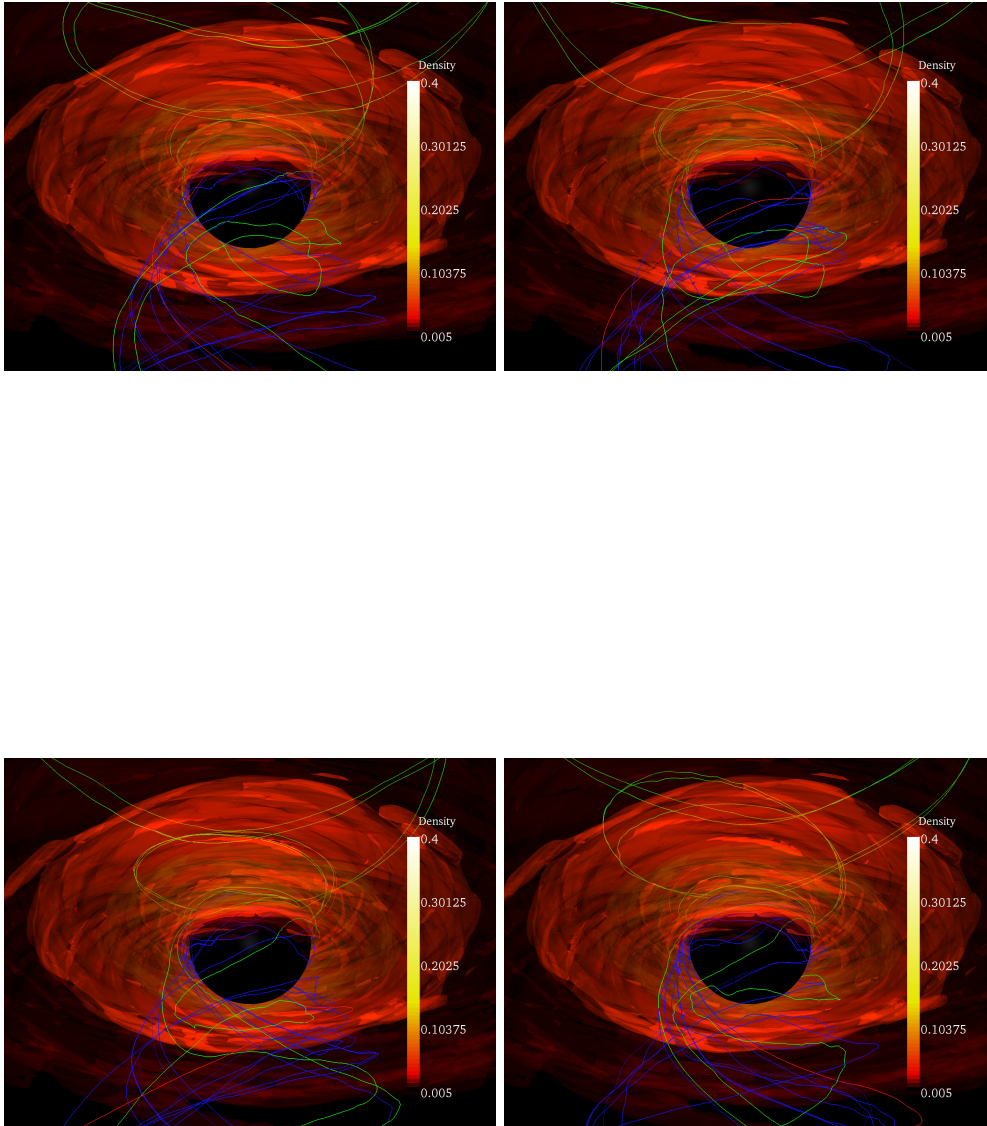


Figure A.17.: The same time slice as Figure 8.16 except that it is shown at different azimuthal angles. The frames are left to right 45 degrees, 135 degrees, in the top row; 225 degrees and 315 degrees in the bottom row, relative to Figure 8.16.

To truly understand the topology of the various field lines one must observe them from different lines of sight since there are always features hidden by the opacity of the density contours and the black hole itself. To this end, we created animations of the camera in Paraview rotating around the black hole. Many of the features can be seen by just showing four frames separated by 90 degrees. Figure 8.17 are frames from an animation as the camera in Paraview rotates around the black hole azimuthally. The frames are left to right 45 degrees, 135 degrees, in the top row; 225 degrees and 315 degrees in the bottom row, relative to Figure 8.16. The rotating camera gives the illusion of the rotating black hole.

A.6. Discussion

This chapter had two topics on the agenda: first to try to convince the reader using new observations and large survey data that the black hole is a more likely power source for FR II jets in quasars than the accretion disk. Secondly, we tried to elucidate the physics of energy extraction from black hole magnetospheres. We showed a very clear simulation of the GHM process that uses relativistic inertia imparted to the plasma by dragging of inertial frames to power a jet at the expense of black hole rotational inertia. The strongest jets that occur in 3-D simulations of horizon magnetospheres are driven primarily by these GHM processes with electrodynamic effects being second order. Thus, the most important astrophysical question seems to be: how much vertical flux can be expected to occur in the equatorial plane of the ergosphere?

There are many physical questions that remain to be answered before a clear picture of black hole driven jets can be universally agreed upon.

1. Does accretion turbulence and resistivity prohibit large amounts of vertical flux through the equatorial plane of the ergosphere?
2. What determines the fraction of jet power that is produced by GHM effects and how much is of electrodynamic origin in the horizon magnetosphere?
3. Can a Blandford-Znajek magnetosphere ever be powerful enough to drive the jets in radio loud quasars?

Bibliography

- Begelman, M., Blandford, R., Rees, M. 1984, *Rev. Mod. Phys.* **56** 255
- Benford, G. 1978, *MNRAS* **183** 29
- Bicknell, G. et al 1998, *ApJ* **495**, 680
- Blandford, R. and Znajek, R. 1977, *MNRAS*. **179**, 433
- Blundell, K., Rawlings, S. 2000, *AJ* **119** 1111
- Bridle, A. et al 1994, *AJ* **108** 766
- Brotherton, M. S., Wills, Beverley J., Francis, Paul J., Steidel, Charles C. 1994, *ApJ* **430** 495
- Camenzind, M. and Khanna, R. 1999, *Nuovo Cimento* **B115**, 815
- Chandran, B., Cowley, S., Morris, M. 2000, *ApJ* **528** 723
- Corbin, M. and Francis, P. 1994, *AJ* **108** 2016
- De Villiers, J-P., Hawley, J., Krolik, 2003, *ApJ* **599** 1238
- De Villiers, J-P., Hawley, J., Krolik, J., Hirose, S. 2005, *ApJ* **620** 878
- De Villiers, J-P., Staff, J., Ouyed, R.. 2005, astro-ph 0502225
- Dunlop, J.S. et al 2003, *MNRAS* **340**, 1095.
- Elvis, M. et al 1994, *ApJS* **95** 1
- Fender, R. 2004 to appear in **Compact Stellar X-ray Sources**, eds W. Lewin and M. van der Klis, Cambridge University Press, astro-ph/0303339
- Garcia, M.R. et al 2003, *ApJ* **591** 388
- Hardee, P. 1996, 3-D simulations of a Cygnus A like jet in Cygnus A - Study of a Radio Galaxy eds. Carilli, C.L. and Harris, D.E. Cambridge University Press New York 113
- Hintzen, P., Ulvestad, J., Owen, F. 1983, *AJ* **88** 709.
- Hirose, S., Krolik, K., De Villiers, J., Hawley, J. 2004, *ApJ* **606**, 1083

- Hawley, J., Krolik, K. 2006, ApJ **641** 103
- Igumenshchev, I.V., Narayan, R. and Abramowicz, M.A. 2003, ApJ **592** 1042
- Koide, S. 2003 Phys Rev D **67** 104010
- Koide, S., Shibata, K., Kudoh, T. and Meier, D. 2002, Science **295**, 1688
- Krolik, K., Hawley, J., Hirose, S. 2005, ApJ **622**, 1008
- Jones, T.J. 2000, AJ **120** 2920
- Kellermann, K. I.; Sramek, R. A.; Schmidt, M.; Green, R. F.; Shaffer, D. B 1994, AJ **108** 1163
- Laor, A. et al 1997, ApJ **477** 93
- Li, L.-X. 2003, Phys Rev D **67** 044007
- Malzac, J., Merloni, A. and Fabian, A. 2004, MNRAS **351** 253
- Meier, D. 1999, ApJ **552** 753
- Narayan, R., Igumenshchev, I. V. and Abramowicz, M. A. 2003, PASJ **55** L69
- Penrose, R. 1969, Nuovo Cimento **1**, 252
- Phinney, E.S. 1983, PhD Dissertation University of Cambridge.
- Punsly, B. and Coroniti, F. 1991, ApJ **350**, 518
- Punsly, B. 1995, AJ **109** 1555
- Punsly, B. 1996, ApJ **473** 152
- Punsly, B. 2001, *Black Hole Gravitohydromagnetics* (Springer-Verlag, New York)
- Punsly, B. and Bini, D. 2004, ApJL **601**, 135
- Punsly, B. 2006, MNRAS **366** 29
- Punsly, B. 2006, ApJL **651** 17
- Punsly, B. 2007, ApJL **661**, 21
- Punsly, B. 2007, MNRAS Letters **381**, 79
- Punsly, B. 2008, *Black Hole Gravitohydromagnetics* second edition (Springer-Verlag, New York)
- Rawlings, S., Eales, S., Riley, J., Saunders, R. 1989, MNRAS **240** 723

- Rawlings, S., Saunders, R. 1991, *Nature* **349**, 138
- Semenov, V. 2002, et al, *Physica Scripta* **65**, 13
- Smith, P., Elston, R., Berriman, G., Allen, R. 1988, *ApJ*, **326** L39
- Telfer, R., Zheng, W., Kriss, G., Davidsen, A. 2002, *ApJ* **565** 773
- Veron-Cetty, M.P., Veron, M. 2001, *Astron. and Astrophys.* **374** 92
- Wang, J, Sulkanen, M. and Lovelace, R. 1990, *ApJ* **335**, 38
- Willott, C., Rawlings, S., Blundell, K., Lacy, M. 1999, *MNRAS* **309** 1017
- Wills, B. et al 1992, *ApJ* **398** 454
- Zheng, W. et al 1997, *ApJ* **475** 469